THE CONTROLLED DRIFT DETECTOR AS AN X-RAY IMAGING DEVICE FOR DIFFRACTION ENHANCED IMAGING

A THESIS SUBMITTED TO
THE GRADUATE SCHOOL OF NATURAL AND APPLIED SCIENCES
OF
MIDDLE EAST TECHNICAL UNIVERSITY

BY

CIGDEM OZKAN

IN PARTIAL FULFILLMENT OF THE REQUIREMENTS
FOR
THE DEGREE OF MASTERS OF SCIENCE
IN
PHYSICS

FEBRUARY 2009

Approval of the thesis:

THE CONTROLLED DRIFT DETECTOR AS AN X-RAY IMAGING DEVICE FOR DIFFRACTION ENHANCED IMAGING

Submitted by **CIGDEM OZKAN** in partial fulfillment of the requirements for the degree of **Masters of Science in Department of Physics, Middle East Technical University** by,

Prof. Dr. Canan Özgen
Dean, Graduate School of **Natural and Applied Sciences** _____

Prof. Dr. Sinan Bilikmen
Head of Department, **Physics** _____

Prof. Dr. Meltem Serin
Supervisor, **Department of Physics, METU** _____

Prof. Dr. Andrea Castoldi
Co-Supervisor, **DEI, Politecnico di Milano, Italy** _____

Examining Committee Members:

Assoc. Prof. Dr. Bahar Dirican
Radiation Oncology Department, GATA _____

Prof. Dr. Meltem Serin
Dept. of Physics, METU _____

Prof Dr Ümit Kızıloğlu
Dept of Physics, METU _____

Assoc. Prof. Dr. Enver Bulur
Dept of Physics, METU _____

Assoc.Prof. Dr Ismail Atılgan
Dept of Physics, METU _____

Date: 06.02.2009

I hereby declare that all information in this document has been obtained and presented in accordance with academic rules and ethical conduct. I also declare that, as required by these rules and conduct, I have fully cited and referenced all material and results that are not original to this work.

Name, Last name: Cigdem Ozkan

Signature :

ABSTRACT

THE CONTROLLED DRIFT DETECTOR AS AN X-RAY IMAGING DEVICE FOR DIFFRACTION ENHANCED IMAGING

Ozkan, Cigdem
M. S., Department of Physics
Supervisor: Prof. Dr. Meltem Serin
Co-Supervisor: Prof. Dr. Andrea Castoldi

February 2009, 63 pages

Diffraction Enhanced Imaging (DEI) is an X-ray imaging technique providing specific information about the molecular structure of a tissue by means of coherently scattered photons.

A Controlled Drift Detector (CDD) is a novel 2D silicon imager developed to be used in X-ray imaging techniques.

In this work a final (complete and detailed) analysis of DEI data taken with the CDD in the ELETTRA synchrotron light source facility in Trieste (Italy) in 2005, is presented and the applicability of both this new technique and the novel detector are discussed.

Keywords: Controlled Drift Detector, Diffraction Enhanced Imaging, Diffraction Enhanced Breast Imaging, Synchrotron Radiation, Coherent Scattering.

ÖZ

X-ISNINLARI GORNTELEME CİHAZI OLARAK KONTROLLÜ DRIFT DETEKTOR'UN KIRINIM YARDIMIYLA KONTRAST'I ARTIRILMIŞ GÖRÜNTÜLEME'DEKİ UYGULANIMI

Özkan, Çigdem

Yüksek Lisans, Fizik Bölümü

Tez Yöneticisi: Prof. Dr. Meltem Serin

Ortak Tez Yöneticisi: Prof. Dr. Andrea Castoldi

Şubat 2009, 63 sayfa

Kontrast'ı Artırılmış Görüntüleme (DEI) bir x-ışınları görüntüleme tekniğidir. Koherent fotonlar aracılığıyla belirli bir dokunun moleküler yapısı hakkinda bilgi verir.

Kontrollü Drift Dedektörü (CDD) 2 boyutta x-ışınları görüntüleme teknikleri icin geliştirilmiş yeni bir silikon aygıtıdır.

Bu calışma, 2005 senesinde ELETTRA sinkrotron ile Trieste'de (Italya) yapılmış DEI deneyinin verileri üzerinde yapılmış tam ve ayrıntılı bir analizi sunulmuştur ve bu yeni dedektörün ve tekniğin uygulanabilirliği ele alınmıştır.

Anahtar Kelimeler: Kontrollu drift dedektörü, Kırınım yardımıyla kontrastı artırılmış meme görüntüleme, Sinkrotron Radyasyon, Kırınım Saçılmalar.

to my mother

ACKNOWLEDGMENTS

I am grateful to my supervisor Dr Meltem Serin for all the effort she invested into the advancement of my academic career at METU.

It has been a privilege working with Dr Andrea Castoldi and Dr Chiara Guazzoni, who patiently taught me about semiconductor detectors, X-ray imaging and Italy, and whose friendship is most valuable to me.

Words cannot describe my gratitude towards my mother Soofia Tahira Elias, to whom I am greatly indebted for everything I have in life, my sister Bilge, my aunts and uncles, whose unceasing support throughout my life has been an integral part of my education. I am also greatly indebted to Francoise and Geoffrey Summers for always being there when the going got really tough, and for Mauritius.

I am grateful for my friends Olga Litvinova, Giorgio Vedani, Chiara Tran, and the grad-school trench buddies: Nuray Er (for the hours spent solving problems concerning Physics and life), Sinem Şaşmaz, Emre, Bengü & Ece “kraliçe” Tasçı and Barış Malcıoğlu (amico di *chai tè con latte* e Venezia).

My special thanks to my bestfriends Grace Akpan & Rebecca Ashurst-Wong for sharing in my laughter and frustrations despite the thousands of miles, and to Andreas Hirstius especially for the supply of wonderful chocolates and comic strips.

I would also like to acknowledge Ms Gülşen Parlak, Ms Zeynep Eke and Ms Sevim Aygar for taking care of the bureaucratic procedures.

TABLE OF CONTENTS

LIST OF FIGURES

LIST OF TABLES

TABLES

CHAPTER 1

INTRODUCTION

X-rays have been among the most important tools for diagnosis and therapy since their discovery by Wilhelm Conrad Röntgen in 1895. X-ray transmission, X-ray diffraction, fluorescence, and Compton scattering are the fundamental effects arising from the interaction of X-rays with matter that can provide information on the structure and composition of the material under analysis. Based on these effects, imaging techniques have been developed for human tissue analysis. The aim of using these techniques is for developing better diagnostic abilities or a better understanding of certain diseases.

Clinical radiography is based on the detection of the transmitted X-rays passing right through the human body and gives information about the densities of the tissues. X-rays, are not only transmitted through the human body in the same direction as their incidence, but may also change their direction within the tissues due to elastic or inelastic scattering. The phenomenon of scattering causes reduction in image quality in radiography in general, and mammography in particular. However, elastically scattered X-rays bear very useful information about the structure of the tissues at the supra-molecular level. Some pathologies, like breast cancer, produce alterations to the molecular structures of the tissues; this alteration is especially evident in collagen-rich tissues.

Diffraction Enhanced Imaging (DEI) is an alternative technique based on utilizing coherently scattered X-rays to generate images that provide higher contrast and specificity than those produced by conventional transmission imaging.This technique is of special interest in cases where the densities of the tissues are very similar (like

in mammography) and the absorption images do not offer enough contrast and this poses a limitation on the interpretation of the image and increases the probability of misinterpretation.

Standard X-ray imaging devices used in clinical radiography are 2D imagers that have a spatial resolution to the order of a few micrometers but fall short in providing a good contrast. According to Oppelt (2005) these devices are X-ray films and digital detectors; whereas digital detectors can be divided into flat panel detectors; such as amorphous-Selenium and amorphous-Silicon Thin Film Transistors (TFT) or photodiodes; and the Charge-Coupled Device (CCD), which is used in slot-scanning systems.

In the previous applications of DEI by CCD, two DEI setups were used, where energy dispersive measurements were carried out separately from the imaging measurements. In the energy dispersive setup a conventional polychromatic X-ray source and an energy dispersive detector (i.e., no spatial resolution) were used to measure the diffraction signature specific to the sample. In order to obtain imaging information a monochromatic synchrotron source was used to irradiate the object and a charge-coupled device camera was used to visualize the high contrast images. Both setups were used to assess the constituents of the sample.

Later, due to its superior energy discrimination capabilities the detection system in the synchrotron DEI setup was upgraded to a novel detector, the Controlled-Drift Detector (CDD). This device developed by Castoldi, Guazzoni, Longoni, Gatti, Rehak and Strüder, looks extremely promising for an application area that requires high contrast. This device is a novel two-dimensional X-ray imager which has a small pixel size comparable to the CCD. However, it is superior to it in certain key areas.

As the developers of the CDD (Castoldi *et. al*) have repeatedly pointed out in their various publications, the incident X-rays in this device are directly converted with high efficiency in the fully depleted silicon bulk, which can be of 300-500 μm thick, and it can measure the energy of the incoming beam with spectroscopic resolution. It can be operated at very high frame rates (up to 100 kHz) and can potentially be

constructed to a large area linear device. This possibility of energy discrimination provided by the CDD allows selection of a narrow momentum transfer window, leading to more powerful experimental implementations of DEI.

An assessment of this upgraded setup was carried out in an experiment at the ELETTRA synchrotron light source facility in Trieste, Italy in 2005. In this experiment, two types of samples were irradiated with the synchrotron beam and the CDD was used to collect data of both techniques: transmission and diffraction images of these samples.

The preliminary reconstruction of the images, obtained from the CDD, showed that it could replace the conventional detection systems.

The objectives of the study reported in this thesis can be outlined as follows:

1. To perform a complete and detailed analysis of the DEI data obtained by CDD of which a preliminary analysis is already available.

2. To assess the performance of the CDD based on the findings of this analysis.

3. To determine the applicability of CDD in X-ray imaging techniques where high contrast is required.

In this study, the detector was calibrated based on the events gathered in each pixel using the synchrotron beam. The calibrated data was used to understand the experimental parameters such as the behavior of the synchrotron beam and intrinsic detector properties such as resolution and drift time.

Imaging data collected for the two samples from the experiment conducted at the ELETTRA synchrotron in 2005 was used to reconstruct these images according to the assessment obtained from the experimental parameters. The two types of samples used for imaging were a Perspex© phantom and pork tissue.

In this introduction chapter, the background information and the objectives of this study, as well as the procedure followed is presented.

Chapter 2 presents the survey of pertinent literature related to basic X-ray interactions, while focusing only on X-ray diffraction imaging techniques based on low angle scattering; and two imaging devices namely, the charge-coupled device and the Controlled-Drift Detector. The experiment held at ELETTRA in 2005 is also introduced in detail.

Chapter 3 presents the material and method of this analysis which is based on the experimental setup used to gather data at the synchrotron.

Chapter 4 presents the results of the final data analysis (performed by the author of this thesis) and a discussion on the comparison of the results.

Chapter 5 concludes the assessment of the applicability of the CDD to diffraction enhanced imaging measurements, along with possible developments to the existing setup and a recommendation for further analysis.

CHAPTER 2

LITERATURE REVIEW

This chapter gives details on the X-ray interactions and imaging techniques; X-ray imaging devices; and application of the CDD to the DEBI technique. Each topic is further subdivided into sections containing relevant information.

2.1. X-Ray Interactions

X-ray radiation has the ability to penetrate materials due to its short wavelength, which makes it an excellent probe to study the structure of materials. The scientific uses vary from medicine to chemistry, also physics and biology. Crystallography, fluoroscopy or radiography, are just a few examples of the use of some of the properties of X-rays as they traverse matter.

The interactions of X-rays with matter depend on the energy of the photons, on the material itself, for example, the average atomic number and its molecular structure. In the X-ray energy range (on the order of 100 eV to 100 keV) photons interact with the electrons of the atomic shell. In the case of photoelectric absorption, a hole is created in the electronic shell, which is filled by another electron from the higher shells. Then either a photon is produced as a radiative process (fluorescence), or non-radiative re-arrangement of the electrons produces the emission of low energy electrons (Auger effect).

Alternatively, the incident photon may scatter elastically or in-elastically. In the latter, the energy of the photon is partially transferred to the scattered photon and an

electron is recoiled in the Compton scattering process. On the other hand, in elastic scattering the energy of the photon is conserved and interferences between wavefronts of the scattered photons are possible. The elastic scattering intensity pattern carries information about the structure of the object at atomic and molecular levels.

In the case of medical imaging, spatial resolution and attenuation determine the suitability of the X-ray region in the electromagnetic spectrum. For the human body the suitable region for imaging is from 0.001 nm to 0.08 nm (1 MeV– 15 keV), where the attenuation is reasonable and the wavelengths are far shorter than the resolution of interest (Keyriläinen, 2004). In diagnostics though, the energy range is limited to the 15-120 keV range where the main X-ray interaction with matter are photoelectric absorption, coherent/elastic (Thomson or Rayleigh) scattering and incoherent/inelastic (Compton) scattering.

a) X-ray Scattering

When diagnostic energy X-rays pass through a material, inelastic scatter, elastic scatter or the photoelectric effect, may take place. The probabilities of these interactions taking place are governed by the X-ray energy and the density and atomic number of the material.

In an inelastic, or Compton, scatter interaction the incoming X-ray interacts with an atomic electron and transfers some of its energy and momentum to that electron, leaving with less energy than it originally had. The probability of this type of scatter occurring in a material is almost uniform at the energies under consideration and the angular distribution of the Compton scattered X-rays is proportional to the differential cross-section per unit solid angle $d\sigma_{inc}/d\Omega$ given by (Hubbell *et. al.*, 1975):

$$\frac{d\sigma_{inc}}{d\Omega} = [S(\chi, Z)]\frac{d\sigma_{KN}}{d\Omega} \qquad (2.1)$$

where the first term, $S(\chi,Z)$, is the incoherent scatter function, which is zero in the forward direction where coherent scattering is dominant, and approaches Z as momentum transfer, χ, is defined by,

$$\chi = \frac{E}{hc}\sin\left(\frac{\theta}{2}\right) \tag{2.2}$$

where h is the Planck's constant, c is the speed of light, E is the energy of the X-rays, and θ is the scatter angle. The second term in equation 1.2 is the Klein-Nishina equation:

$$\frac{d\sigma_{KN}}{d\Omega} = \frac{r_0^2}{2}(1+\cos^2\theta)\left(\frac{1}{1+\alpha(1-\cos\theta)}\right)^2\left(1+\frac{\alpha^2(1-\cos\theta)^2}{[1+\alpha(1-\cos\theta)](1+\cos^2\theta)}\right) \tag{2.3}$$

r_0 is the classical electron radius and α is the ratio of the photon energy to the rest mass of an electron.

Coherent scattering is described classically as the interaction between the electric field associated with the X-ray beam and the electric field associated with the electron charge distribution in the material (Roy *et. al.*, 1999). The electrons are set oscillating and subsequently emit radiation of the same wavelength as the incident beam.The differential cross-section per unit solid angle of the exiting radiation is given by Johns and Cunningham (1983):

$$\frac{d\sigma_{coh}}{d\Omega} = \frac{r_0^2}{2}(1+\cos^2\theta)[F(\chi,Z)]^2 \tag{2.4}$$

where r_0 is the classical electron radius, $(1+\cos^2\theta)$ arises from averaging over all possible polarizations and $F(\chi,Z)$ is the coherent scatter form factor which is a function of momentum transfer and the atomic number of the scatterer. Conversely to the incoherent scatter form factor, the coherent scatter form factor, F, tends towards zero for large values of θ.

The probability of a photon being scattered per unit length of beam path, which is the theoretical linear differential scattering coefficient is given as (Tartari, 1999),

$$\mu_s(E,\chi) = \frac{N_A \rho}{M}\left(\frac{d\sigma_{coh}}{d\Omega} + \frac{d\sigma_{inc}}{d\Omega}\right) \tag{2.5}$$

where N_A is the Avogadro constant, M is the molecular weight and ρ is the density of the material.

Equation 2.5 indicates that at diagnostic energies the scattered X-rays predominantly follow paths at a small angle to the original direction of travel. A simple model of this situation is seen in the theory of Bragg scattering in regular crystals and a more complex treatment occurs in semi-regular structures, such as biological tissues (Griffiths, 2005).

2.2. X-Ray Imaging Techniques

X-ray interactions mentioned in the preceding sections have been utilized for imaging human tissues in order to develop a better diagnosis and understanding of diseases. The techniques vary according to the type of interaction from radiography to diffraction imaging.

2.2.1. Radiography

Radiography is the first known application of X-rays after their discovery by Röntgen in 1895. He was the first to apply this radiation to non-invasive and in vivo medical examination.

To obtain a radiographic image is fairly simple as a source of X-rays illuminates an X-ray sensitive film situated just behind the object. The intensity of the X-rays passing through the object is related to the absorption and to the thickness of the object. This intensity is recorded on a film which is developed for visual assessment.

Radiographs of bones have in general good contrast because bones absorb the photons more than the surrounding soft tissues. Therefore, the X-rays are a great help in traumatology. The situation changes in imaging soft tissues where their densities

are very similar and their absorption coefficients are very close to each other and offer little contrast. One way avoiding this is to add a contrast agent (higher absorption coefficient) into the body cavities or injecting into the vascular system. As a result, the structures of the body appear contrasted against the surrounding tissues.

Radiographs are commonly obtained using polychromatic sources (X-ray tubes). The low-energy part of the spectrum emitted by the source does not contribute to the image formation but deposits dose on the object. Synchrotron radiography allows the use of almost totally monochromatic radiation, increasing the quality of the image reducing the dose delivered to the object.

2.2.2. Diffraction Enhanced Imaging

Presented here are two X-ray diffraction enhanced imaging (DEI) methods based on coherent scattering for low angles (up to 10^{o}). Other diffraction imaging techniques are not taken into consideration.

2.2.2.1. DEI based on Analyzer Crystal

Obtaining a good contrast in radiography of biological materials with similar elemental composition can be difficult, especially at high photon energies. Absorption does not yield enough contrast to differentiate areas of the object with very similar densities and in such cases diffraction imaging may play an important role.

X-ray diffraction from perfect crystals, with narrow reflection angular width (on the order of a few microradians) and peak reflectivity of close to unity, provides the tools necessary to prepare and analyze X-ray beams that traverse an object on the microradian scale (Pisano *et. al.*, 2000).

The condition for X-ray diffraction from a crystal is met only when the incident beam makes the correct angle to the atomic lattice planes in the crystal for a given X-

ray energy or wavelength. When this condition is met, the beam diffracts from the planes over a narrow range of incident angles. When constructive interference between scattered waves takes place at certain angles, the Bragg effect or X-ray diffraction occurs. The angles, at which the interference between the waves occurs are given by the Bragg condition:

$$n\lambda = 2d \sin \theta_B \tag{2.6}$$

Where n is an integer and refers to the order of diffraction, λ is the wavelength, d is the interplanar spacing and θ_B is the Bragg angle. The interference between the waves scattered from the electrons within the same atom, molecule and neighbouring molecules result in a diffraction pattern related to the spatial distribution of electrons.

As the crystal is rotated about an axis parallel to the lattice planes and perpendicular to the incident beam direction, an intensity variation is observed. This is referred to as the *rocking curve*, which is shown in Figure 2.1 below. The shape of this curve is roughly triangular, with the peak reflectivity approaching nearly 100% (Chapman *et. al*., 1997).

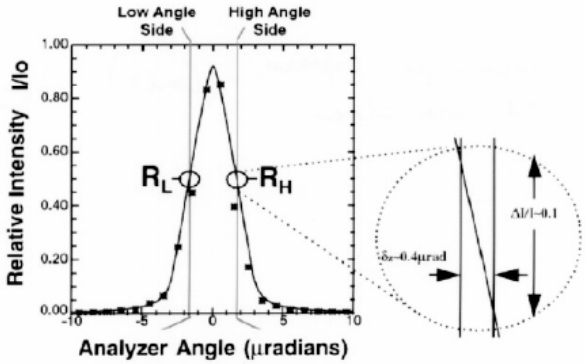

Figure 2.1:Rocking curve of a Silicon crystal analyzer (Vedani, 2007)

In Diffraction Enhanced Imaging, an imaging beam is prepared by means of diffraction of the polychromatic beam from the synchrotron on a monochromator crystal to create a nearly monoenergetic imaging beam. This beam is then passed through the object being imaged as in conventional radiography. However, a matching crystal is placed between the object and the detector. This crystal is set at or near the peak of Bragg diffraction and is called the analyzer crystal. A schematic representation of a synchrotron radiography and diffraction-enhanced imaging system is shown in Figure 2.2 (Pisano *et. al*., 2000).

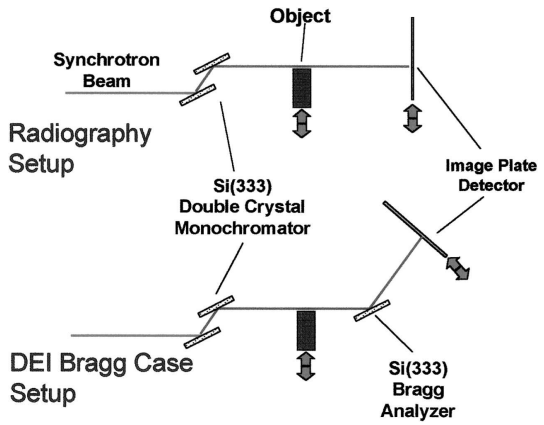

Figure 2.2: A schematic representation of a synchrotron radiography and Diffraction Enhanced Imaging system (Pisano *et. al*., 2000).

Since the condition for diffraction from this analyzer crystal limits the X-rays that can be diffracted into the detector, it automatically provides a high degree of scatter rejection, which results in improved image contrast. The range of angles accepted by the analyzer crystal is a few microradians, which provides scatter rejection better than conventional anti-scatter techniques such as slit collimation and grids (Chapman *et. al*., 1997).

The improved image contrast obtained by means of scatter rejection is called *extinction contrast*, a term used in optics and X-ray diffraction to describe intensity loss due to diffraction and scattering. Therefore, the image that represents the

absorption of the object by X-rays is referred to as the *apparent absorption image*, since it has contrast derived from both absorption and extinction (Pisano *et. al*., 2000).

The DEI reconstruction consists of an algorithm that retrieves the apparent absorption from the two images recorded, from each pixel, when the analyzer crystal is tuned. “This image contrast source may be further developed to apply to medical and biologic imaging” (Chapman *et. al*., 1997).

2.2.2.2. DEI based on using Mechanical Collimation

Breast cancer alters the structure of the tissues, being especially evident in collagen-rich tissues. However, detection of a tumor by means of conventional radiography is not easy since the densities of the tissues are very similar and the absorption images do not offer enough contrast. While a tumor can be easily detected in a predominantly fatty breast due to the large difference in the attenuation coefficients of the two tissue types, the detection of a tumor in a denser breast becomes difficult due to the small difference in the attenuation coefficients of carcinoma and of fibroglandular tissue as reported by Johns and Yaffe (1987).

Diffraction Enhanced Breast Imaging (DEBI) is a technique developed to investigate elastic, or coherent, scatter from human breast tissues with a view to incorporating a scatter detector into a standard mammographic unit or creating an X-ray diffraction imaging biopsy tool in the future (Griffiths, 2005).

There have been several studies examining the diffraction signatures of various biological tissues, with breast tissue being measured by groups such as Evans *et. al.*(1991), Kidane *et. al.*(1999), Lewis *et. al.*(2000) and Poletti *et. al.*, (2002). The authors, who considered signals at momentum transfer values between 1.0 and 3.0 nm^{-1}, have all seen differences between the signals for fatty and non-fatty tissues, although this work has been limited by the inhomogeneous nature of the tissue samples. Some initial work was also carried out in order to investigate the feasibility of using elastic scatter to form images of breast tissue phantoms with a charge-

coupled device camera (Harris *et. al.*, 2003). Based on the success of this work further investigation was directed towards analysis of the diffraction signatures of breast tissues of and diffraction imaging by Griffiths (2005).

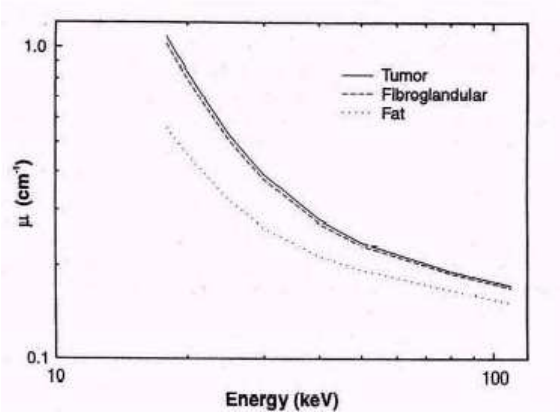

Figure 2.3: Graph representing the absorption coefficients of three different types of breast tissue (Vedani, 2007).

In biological materials coherent scatter becomes important at photon energies below 50 keV and, because of its sharply forward peaked nature it is the dominant scattering process at low angles. The interference of scattered photons gives rise to diffraction patterns. These patterns provide a unique signature characteristic of the material that has been irradiated. In the case of a structure with a short-range order, such as biological tissue, the distribution of the scattered intensity is characterized by one or more smooth peaks at well-defined values of the momentum transfer given in equation (2.2).

Figure 2.4 shows the scattered signal from breast tissue. As it can be seen from the figure, normal tissue peaks at χ =1.1 $nm^{-1}$and carcinoma peaks near χ = 1.7 nm^{-1}."At χ = 1.1 nm^{-1}, the signal from normal tissue is about twice the signal from carcinoma, while at χ = 1.7 nm^{-1} the diffracted intensity from carcinoma is about 1.5 times higher than that from healthy tissue. At χ = 1.3 nm^{-1}, the signal from normal tissue is nearly equal to the signal from carcinoma" (Castoldi *et. al.*, 2007).

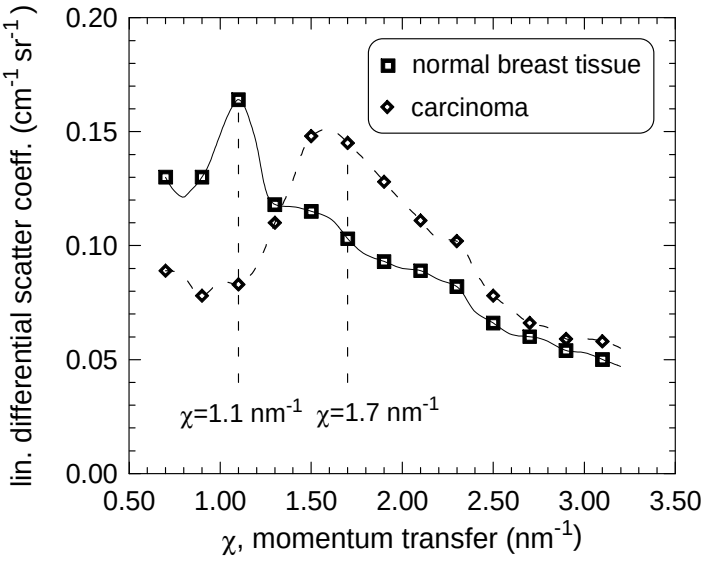

Figure 2.4: Linear differential scatter coefficient of carcinoma versus normal tissue for at different momentum transfer values Diffraction highlights the difference between carcinoma and healthy breast tissue (Castoldi *et. al.*, 2007).

Earlier DEBI experiments were carried out in two steps where energy dispersive measurements were carried out separately from the imaging measurements.

a). Energy Dispersive Setup

A schematic representation of the setup used in Energy Dispersive DEBI is shown in Figure 2.5a. A polychromatic X-ray pencil beam was used to illuminate the sample and the photons scattered at a given angle were selected with a conical collimator and detected with an energy dispersive detector (for e.g. HPGe detector). The main advantage of this technique is the use of a conventional source as the primary beam as it allows investigating several momentum transfer values simultaneously. Unfortunately, the technique has no position discrimination capability; therefore it can be used in the study of homogenous media to determine the material linear differential scatter coefficient of the sample being studied. This technique has a major drawback; it does not provide imaging information unless the sample is scanned in front of the beam, which implies longer acquisition times.

b). Synchrotron Radiation Setup

A schematic representation of the setup used in imaging measurements carried out in the synchrotron is shown in Figure 2.5b. The primary radiation is a monochromatic laminar beam from a synchrotron source. A position-sensitive detector, coupled to a multi-hole collimator, is used to gather the record diffraction images at different values of the momentum transfer by changing either the beam energy or the scatter angle θ. The implementation of this technique with conventional X-ray sources imposes strict requirements on the detector side in terms of energy and position resolution. A low noise level charge-coupled device (CCD)camera (Jerram *et. al.*, 2001) used for this setup had a very good position resolution (to the order of tens of micrometers), but featured no energy discrimination capabilities.

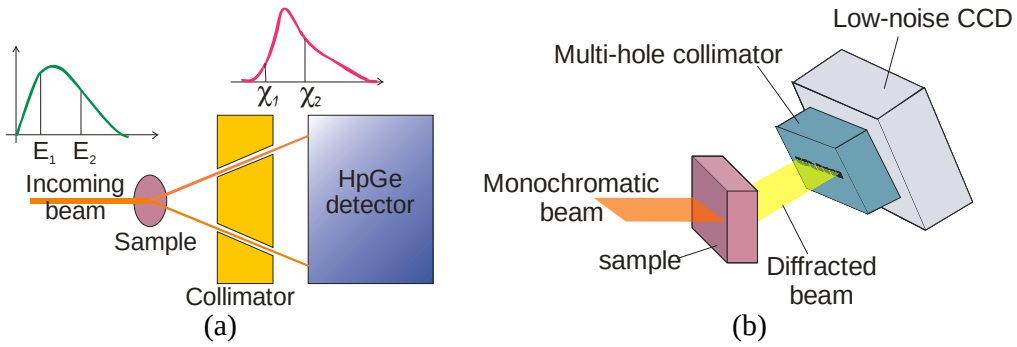

Figure 2.5: (a) Schematic diagram of the setup used in Energy Dispersive DEBI.(b) Schematic diagram of the setup used in Synchrotron Radiation DEBI experiments (Castoldi *et. al.*, 2007)

The main challenge in developing imaging devices suited for diffraction enhanced imaging arises from the requirement of a system with good spatial resolution and high contrast sensitivity. The spatial resolution is partly dependent on the pixel size of the detector. In the case of the charge-coupled device the spatial resolution can go down to few tens of microns. However, higher spatial resolution has no significant effect on the diagnostic accuracy in the characterization of micro-calcification, although detection accuracy can be reduced with the pixel size. In addition to good

contrast performance, the identification of small-size low-contrast objects is characterized by the ratio of contrast to background noise. Hence, both spatial resolution and contrast are of paramount importance in cancer detection.

The main limitation of DEI is the low yield of scattered photons for a given angular aperture. For this reason, the choice of a suitable detector is crucial.

2.2.2.3. Requirements of the Detection System

There are several criteria for selecting a suitable detector for DEI. The detector has to be able to clearly observe signal above the background that will be present from the noise intrinsic to the detection system. The number of coherently scattered X-rays reaching the detector in a diffraction system will be small compared to the number of X-rays being produced at the source. This is due to the probability of a coherent scatter taking place and also the diagnostically useful coherent scatter signal is further defined by the system collimation (Griffiths, 2005). The total useful signal in the diffraction system comes from just a small number of X-ray photons. Thus the scatter detector must have high quantum efficiency in order to physically capture the signal from as many of the photons that reach it as possible. Once a photon has interacted with the detector, then its signal must compete with the noise within the detector and its associated electronics. Therefore, a detector with readout noise negligible with respect to intrinsic noise due to charge generation would ideally be required to detect individual X-rays.

Spatial resolving capabilities also play a part in detector choice. If the detector has no spatial resolution then scatter data can be recorded from just one collimation defined voxel at a time (Griffiths, 2005). This is adequate for small samples, but is not a practical situation when wishing to cover a large area to be imaged in a reasonable time.

A detector that is used for diffraction imaging should have spatial resolution capabilities at least of a similar order of magnitude to the collimation so that data is not lost. A large imaging area/field of view would obviously also be an advantage for

the detector such that a large area phantom can be imaged quickly, however, providing that a number of the individual detectors could be tiled, this is not such an important issue.

As mentioned in sections 2.1.3.2a and 2.1.3.2b, a charge-coupled device camera and a high purity Germanium detector was used in the earlier experiments to tackle the limitations of DEI.

There exists a device that looks particularly promising for such an application where contrast is of the utmost importance. This device is the Controlled-Drift Detector, CDD. As repeatedly mentioned by Castoldi *et al*, the CDD is a novel Silicon 2D X-ray imager, which works in the single photon counting mode so, the energy and incident position of each incoming photon can be individually measured with small noise intrinsic to the detector. The X-rays are directly converted in the silicon bulk with thickness 300-500μm, which is fully depleted of the mobile carriers leading to a high detection efficiency in the 1-20keV range. The CDD has a pixel size comparable to a charge-coupled device and it can measure the energy each individual incoming X-ray with spectroscopic resolution, at very high frame rates. It can also be constructed to a large area linear device. The possibility of energy discrimination provided by the CDD allows selection of a narrow momentum transfer window, and use of polychromatic X-ray generators leading to more powerful experimental implementations of DEI (Castoldi e*t al*, 2007).

2.3. X-Ray Imaging Devices

In conventional mammography the requirements for the components of the imaging system are very high. The X-ray source must provide a soft X-ray spectrum as it is needed for high radiographic contrast. If too soft a spectrum is used, then the lower-energy photons contribute only to dose, not to contrast (Keyriläinen, 2004). The size and shape of the focal spot of the X-ray source and intensity distribution of the X-rays along with the beam geometry determine the spatial resolution achievable and the visualization of small-sized objects. However, this is an issue when concerning

long acquisition time. Additionally, the diverging incident beam produces scattered radiation that degrades contrast by adding uniform noisy background to the image.

Oppelt (2005) has mentioned that thirty to forty years ago diagnostic X-rays were recorded on direct exposure films for mammograms. Direct exposure industrial X-ray film has low absorption efficiency for photons in the diagnostic energy range and thus requires long exposure times leading to high absorbed doses. Currently screen-film systems have replaced the earlier devices. New digital systems are being continuously introduced and different techniques are used to convert the energy distribution deposited on the receptor into a visible image (Oppelt, 2005).

The recent introduction of the digital detectors to mammography systems has allowed the improvement of image quality. Early experience demonstrated the potential of these detectors for reducing the number of false-positive biopsy results (Keyriläinen, 2004). Additionally they have been of great advantage for early detection and determination of lesion type and size. Digital technology enables separation of the functions of image acquisition, display and storage so that each can be optimized independently. As a result of better absorption efficiency of the incident photons, and lower system noise, digital mammography enables dose reduction by adjusting dose to give the required noise level in the image. Also, a consistent response to radiation significantly eliminates the need for a second acquisition (Keyriläinen, 2004).

Digital image processing technology also allows implementation of assisting tools such as computer aided detection and diagnosis. Specially tailored algorithms may improve the detection of different types of abnormal mammographic signs.

The main challenge in these devices arises from the requirement for a system with good spatial resolution and high contrast sensitivity. This is partly dependent on the pixel size of the detector. The major problem is to accomplish all this with areas comparable to screen-film systems.

One of the popular imaging devices being used in achieving high spatial resolution in digital detection is the Charge-Coupled Device.

2.3.1. The Charge-Coupled Device

The Charge-Coupled Device is a metal-oxide semiconductor (MOS) structure which can collect charge in localized potential wells. It is characterized in a structure to develop a matrix of potential wells, or pixels, in which charge is collected and transferred to the output nodes. This 2D matrix allows rebuilding the position of the charge with precision depending on the pixel size (Theuwissen, 1995).

The charge-coupled device is, generally, an epitaxial layer of silicon which has a doping of p+ (Boron) and is grown upon the substrate material. In buried channel devices, the type of design utilized in most modern charge-coupled devices, certain areas of the surface of the silicon are ion implanted with phosphorus, giving them an n-doped designation. This region defines the channel in which the photo-generated charge packets will travel. The gate oxide, i.e. the capacitor dielectric, is grown on top of the epitaxial layer and substrate.

According to Davidson and Abramowitz (2006), the charge transfer through the shift registers occurs after integration to relocate accumulated charge information to the sense amplifier, which is physically separated from the parallel pixel array. The two phase technique illustrated in Figure 2.6, is one of the clocking methods utilized to transfer charge from the collection gates to the output node. A two phase charge transfer clocking scheme employs four gates for each pixel, with adjacent gates connected together as pairs. Each gate pair is connected to an alternate clock line and one of the gates in each pair is designed with an increased n-type doping level beneath the gate. When voltage is applied to the gate pair, the gate having the increased doping level has a more positive potential, which increases the depth of the charge storage area and results in a step in the potential energy profile.

The same authors state that the nature of electrostatic forces in the silicon substrate beneath the gates is determined by the voltage level applied to a particular gate by the clock input signal. High level voltages induce the formation of a potential-well beneath the gate, whereas low level voltages form a potential barrier to electron movement. Clock lines are alternately pulsed, resulting in the charge packets being

shifted along the device in a direction that is determined by the position of the extra doping.

The initial state, shown as the first set of steps in Figure 2.6 is with the combined gates at φ_1 having a low-level voltage forming a pair of stepped potential barriers, with the potential higher in the region beneath the gate having the increased doping level. At the same time, the combined gates at φ_2 have a high-level voltage and form stepped potential wells, in which the deepest well appears beneath the gate having a normal doping level. At the next state as shown in the second set of steps in the Figure 2.6, to complete the short cycle the voltage levels are reversed with the gates at φ_1 having the high-level voltages (and the potential wells) and the gates at φ_2 having the low-level voltages (Abramowitz and Davidson, 2004).

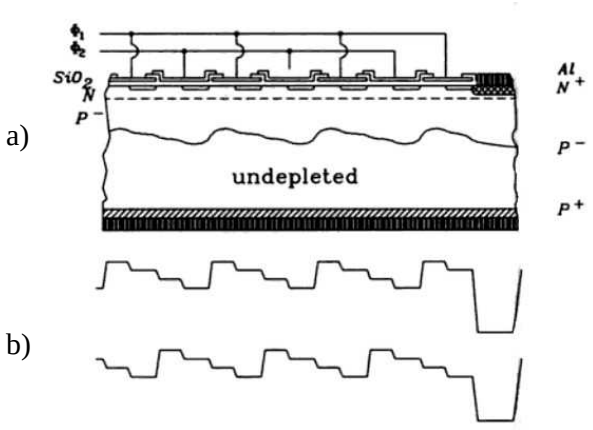

Figure 2.6: Two phase Charge-Coupled Device with built-in transfer direction (a)cross section (b) potential along transfer direction (Lutz, 1999).

The image is obtained by alternating between these two phases (integration and readout) and adding the events recorded in every pixel. Therefore the acquisition time of a frame is given by the sum of the integration time and the time required to transfer and read-out the full gate array (single output channel). Since the content of every pixel should be transferred and tried, the total time of reading of a column

depends on the sum of the transfer time of the contents of a pixel into the adjacent one T_{tr} with the processing time T_{proc}, multiplied with the number of pixels.

$$T_{readout} = N_{pixel} (T_{proc} + T_{tr}) \quad (2.7)$$

It should be noted that the time required to measure the signal charges of all pixels is dominant, for reading depends directly on the processing time and the number of pixels in each column, and therefore the dimensions of the detector. (Galimberti, 2004)

This possibility of 2D reconstruction along with the pixel size (on the order of tens of microns) dictating the spatial resolution, makes the charge-coupled device a good candidate for X-ray imaging. However, the device itself has a rather low sensitivity to X-rays and has to be combined with a scintillating film. A scintillating layer is a layer composed by a material that produces visible light when the X-rays hit it. The scintillator should enable high X-ray absorption efficiency and emit at a wavelength suitable to the charge-coupled device's sensitivity. A drawback of this approach is that the spatial resolution of the device is approximately equal to the thickness of the scintillating layer, i. e., a thicker scintillating layer absorbs more X-rays and depreciates the spatial resolution (Rowlands, 1998).

Another drawback of the charge-coupled device is the slowness of the reading which is on the order of seconds for a single channel output or milliseconds for a multicolumn readout. The readout time limits the obtainable temporal resolution, which means using longer integration times. Longer integration time means larger leakage charge whose fluctuations add to the noise (Galimberti, 2004).

2.3.2. The Controlled-Drift Detector

The Controlled Drift Detector (CDD) is a fully depleted silicon detector that allows 2D position sensitive X-ray imaging in the 1-20 keV energy range. It was proposed by Castoldi *et. al.* (1997), in the frame work of a long-lasting collaboration between Brookhaven National Laboratory (USA), Max Planck Institute (Germany),

Politecnico di Milano (Italy) and INFN-Sezione di Milano (Italy). the first experimental evidence of its working principle was reported in (Castoldi *et. al.*, 2000a).

2.3.2.1. Working Principle

The Controlled-Drift Detector is operated in the integrate-readout mode.

- Integration mode: During this mode the drift of the signal is blocked and the signal charge is fully confined in a matrix of potential wells.
- Drift mode: The transition to this mode is achieved by removing these potential barriers defining the pixels by externally applying a small voltage to the suitable electrodes. The signal charge is then swept towards the readout electrode situated at the end of each column by a uniform electrostatic field. The design of potential lateral barriers prevents the broadening of the signal charge along the direction transversal to the drift.

The position of the irradiated pixel is given by the time between the start of the drift mode and the measured arrival time of the signal electrons to the readout electrode. The second coordinate is obtained providing a separate readout electrode for each pixel column (Guazzoni, 1997, Castoldi et. al. 1997a).

The energy of each detected photon is given by the measurement of the collected charge, i.e. the amplitude of the signal at the anode (Guazzoni, 1997, Castoldi et. al. 1997a).

The duration of the readout phase must be equal to or larger than the drift time of the signal charge. The nominal drift velocity is given by the applied drift field multiplied by the bulk mobility.

$$\nu_d = \mu_n E_{drift} \tag{2.8}$$

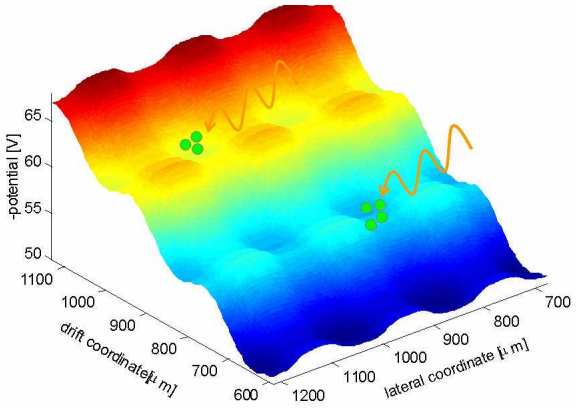

Integration Phase

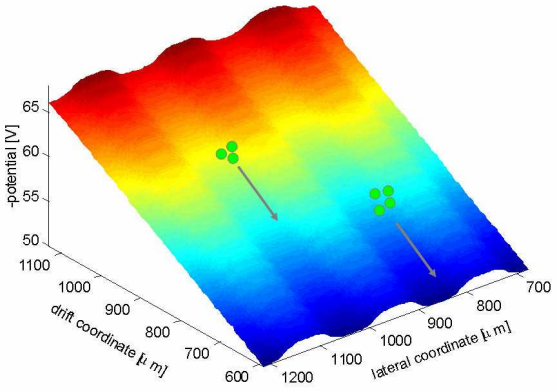

Drift Phase

Figure 2.7: 3D simulation of the potential wells for the integration and drift modes for the Controlled-Drift Detector in a plane parallel to the detector surface at a few micrometers from the anode side (Galimberti, 2004)

This transport mechanism based on the electrons drift has three major advantages:

- it reduces dramatically the number of channels required for true 2D position sensing (i.e. number of columns, not the number of pixels),
- it leads to readout times of only a few microseconds and
- it naturally allows the connection of the front-end electronics at the side of the detector chip, thus simplifying the interconnection issue.

The deposited energy can be measured with spectroscopic resolution at (or very close to) room temperature with an energy resolution dependent on the leakage current.

2.3.2.2. Implementation

The CDD is realised on a high-resistivity n-type substrate which is fully depleted by many shallow p+ electrodes realised on the top side of the detector called strips and by one or more p+ electrode on the backside. The incremental bias voltage of these strips generates the electrostatic field during the drift phase. This field is active and drifts the signal charges to the n+ collecting anode where the charges are read (Galimberti, 2004).

A lower resistivity n-type epitaxial layer is present to displace the potential minimum for electrons at a depth of few microns below the top surface. In this way the signal charges can be influenced by the surface potential, allowing control of the potential barriers needed by this detector (Castoldi *et.al.*, 1998, 1999, 2000b).

The realised deep p+ implants, called channel-stops create permanent local maxima of the potential along the normal of the drift direction that allows the division of the detector into independent drift channels each with its own readout anode. In the same way the externally controlled potential barriers that enable/disable the drift can be realised by modifying the surface potential of the top side (Castoldi *et. al.*, 1995, 1996, 1997b).

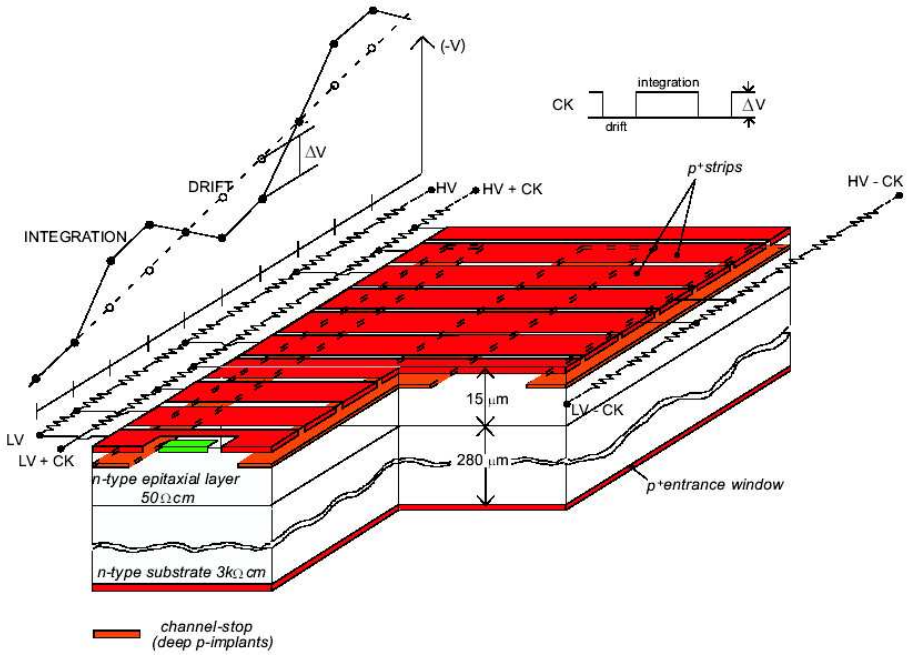

Figure 2.8: Implementation of the Controlled-Drift Detector. The p+ deep implants called channel stops, divide the active area into independent drift columns, each with its own readout anode. The inset shows the diagram of the bias potential of the strips of during integration mode (Guazzoni, 1997).

The potential barriers are obtained by superposing a quasi-sinusoidal perturbation of amplitude ΔV to the linearly increasing bias voltage of the strips. When applied, this bias perturbation generates the needed potential barriers whose amplitude can be adjusted by ΔV. One way to easily generate and remove this biasing scheme is to bias the strips by means of three integrated resistive dividers, alternatively connected to the strips as shown in Figure 2.9 (Guazzoni, 1997).

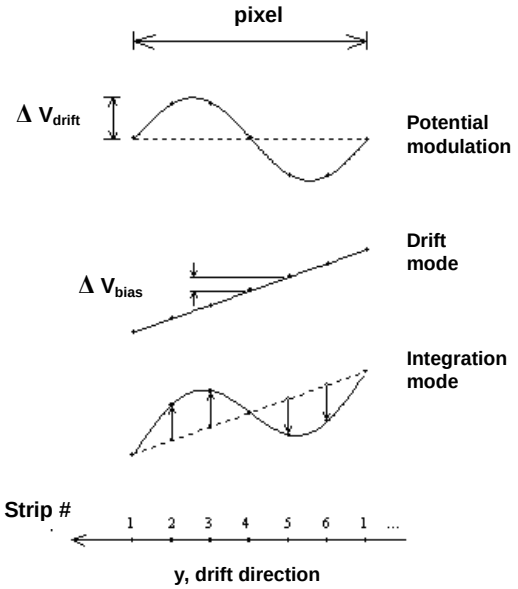

Figure 2.9: The external potential barriers along the drift direction are obtained by mismatching the bias of the three resistor networks (Guazzoni, 1997).

Guazzoni (1997) explains the biasing mechanism, where in the drift phase the resistive dividers are biased at the same voltage so that the strips are biased at linearly increasing potential generating the uniform electrostatic field. By mismatching the voltages of these dividers - i.e. by adding ΔV to the first divider, subtracting ΔV from the second and leaving the third unchanged - the quasi-sinusoidal perturbation is created and the drift of the charges is blocked.

The signal charges in the CDD are readout simultaneously by a uniform electric field. The total readout time required is fixed by the maximum drift time of the charge T_{drift}. This time is related to the drift velocity of the charges and the length of the drift column. Therefore the minimum readout time of the CDD is equal to the duration of the drift stage,

$$T_{readout} = T_{drift} \tag{2.9}$$

The readout time does not depend on the processing because the integration phase can be started just after the collection of all the pixel charges is complete.

The readout time in a detector sets the minimum allowable duration of the integration phase and then the maximum frame frequency:

$$F_{frame} = 1/(T_{readout} + T_{int}) \quad (2.10)$$

As in the charge-coupled device, the photons collected by the active area while the detector is in readout phase generate erroneous position attribution. To keep these erroneous events to a minimum with respect to the correctly acquired events, the ratio between the integration and the readout time is typically on the order of ten (Galimberti, 2004).

The frame rate of the CDD allows working at a frame frequency nearly two orders of magnitude greater than the frame frequency of the charge-coupled device. This attribute is better suited for time resolved analysis of fast varying X-ray sources.

2.3.2.3 Integrated Electronics

Each anode of the CDD has integrated front-end electronics composed by two n-type Junction Field Effect Transistors (nJFET), called First FET and Reset FET. The First FET is connected in a source-follower configuration to buffer the signal generated by the charge on the anode of the chip from the large stray capacitance of the external connection. In this way the anode capacitance is kept very small (about 0.1pF) which improves the noise performance of the detector. The main task of the Reset FET is to bias the anode at a very-high equivalent resistance so as not to introduce significant parallel noise (Galimberti, 2004).

The readout chain is a conventional chain composed of a low-noise high-speed preamplifier followed by a unipolar Gaussian shaping amplifier.

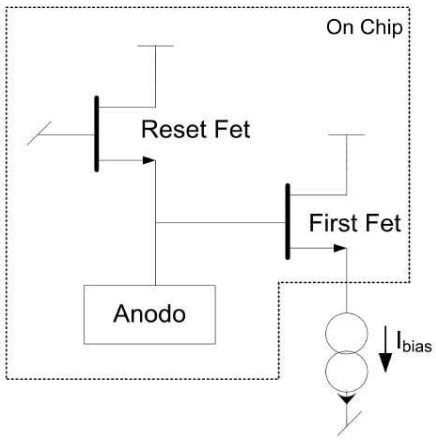

Figure 2.10: Schematic of the on-chip electronics. The First FET reduces the anode capacitance, in-turn reducing the noise performance and the Reset FET keeps the anode biased at high resistance (Galimberti, 2004).

2.3.2.4. Detector Performance

The achievable performance of the CDD had been assessed in earlier studies in terms of energy resolution position resolution and maximum event rate. A dedicated data acquisition system was developed which is explained in section 2.3.2.

Figure 2.11 shows the position-sensing and spectroscopic capabilities of a CDD column (pixel size 180µm x 180µm) irradiated with a ^{55}Fe source (Castoldi *et.al.*, 2006).

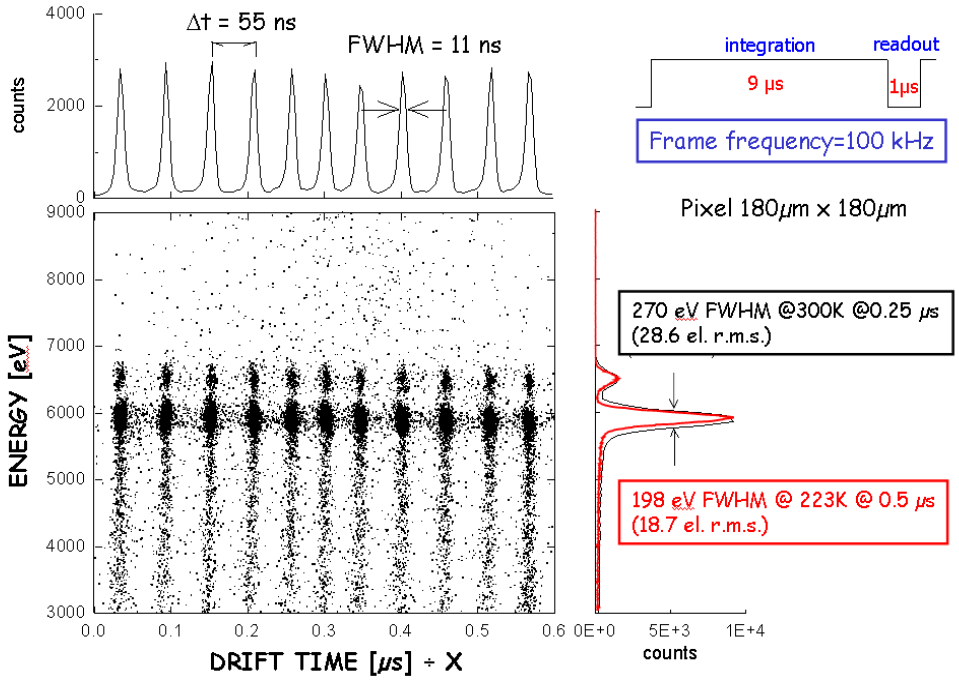

Figure 2.11: Scatter plot of the energy versus drift time of the X-rays of a ^{55}Fe source collected by irradiating column of the CDD at 100 kHz frame frequency at room temperature. The inset on the right shows the energy spectrum of all the events at 300 K and 223 K. The top insert shows the event distribution along the drift times, i.e., along the drift coordinate (Castoldi *et.al.*, 2006).

The detector was operated at 100 kHz frame frequency where the time duration of the drift/readout mode was set to 1 µs and the time duration of the integration mode was set to 9 µs. Scatter plot shows the drift time versus energy of the detected X-ray events. Along the vertical axis it can be seen that the events are clearly gathered around the characteristic energy lines emitted from the ^{55}Fe source. Along the time axis, the drift times corresponding to the individual pixels are nicely separated, demonstrating the one dimensional position sensing of the detected X-rays.

The energy resolution of the tested prototype at 5.9 keV was 277 eV FWHM and 198 eV FWHM at 300 K and 223 K respectively.

2.3.2.5. X-Ray Imaging using the CDD

Presented here is the result of an earlier study, from Castoldi *et. al.* (2006), where the application of the CDD in X-ray imaging experiments was carried out with synchrotron light at SYRMEP beam-line of the ELETTRA Synchrotron in Trieste (Italy). The prototype used in this application had a pixel resolution of 120 µm x 120 µm and featured 13x14 pixels. It was operated at 100 kHz frame frequency at room temperature.

Figure 2.12 shows the X-ray image of a lizard obtained by accumulating 150 000 frames by panning out the detector to cover the imaged area. The energy of the incident beam was set to 15 keV, which was high enough to pass through the lizard's organs. The details in the lizard body are resolved enough to distinguish the vertebral column, rib bones and even a faint image of the lungs. The two black spots on the radiograph are due to small stones that were present in the lizard's body.

The energy spectrum of the photons collected in each pixel can be obtained easily. "This feature can be used to exclude inelastic scattered photons that can spoil the contrast of the acquired image" (Castoldi *et. al.*, 2006).

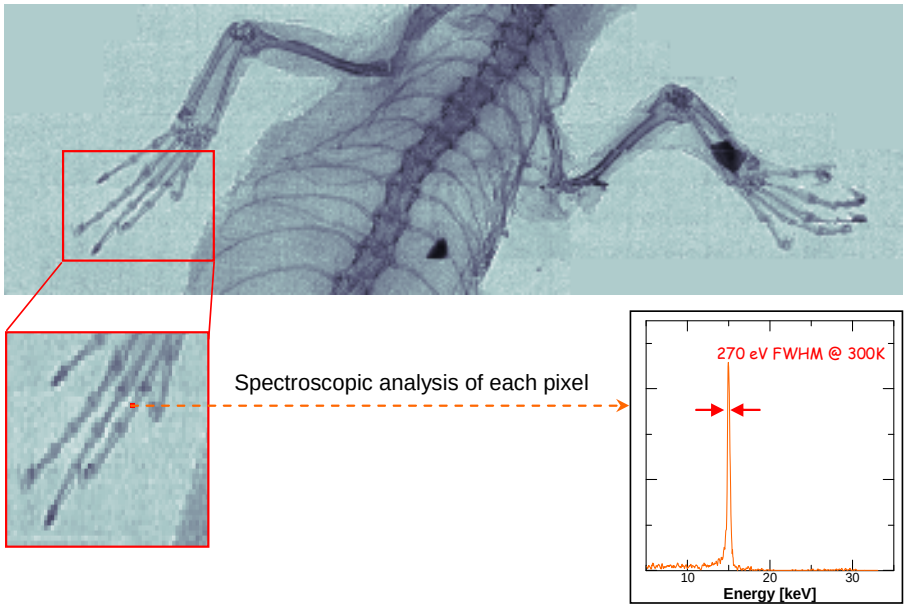

Figure 2.12: X-ray radiographic image of a lizard acquired with a CDD operated 100 kHz at frame frequency, at room temperature. The image is obtained accumulating 150,000 frames. The energy of the incident beam was set to 15 keV (Castoldi *et. al.*, 2006).

2.4. Application of the CDD to DEI

The assessment of the Controlled-Drift Detector in diffraction enhanced imaging of tissues, was first carried out at the SYRMEP beam-line at the ELETTRA synchrotron in Trieste, Italy (2005). The Controlled-Drift Detector prototype used for the study had a 180 µm × 180 µm pixel size and a total area of 3.96 mm × 6.12 mm which means 22×34 pixels (Vescovi, 2005). Two beam energies were used to define the required momentum transfer values of interest, which are 18 keV for χ=1.1 nm^{-1} and 26 keV for χ =1.7 nm^{-1}, for the chosen diffraction angle. The detector thickness was 300 µm, which allows a photon absorption efficiency of about 30% at 18 keV and 14% at 26 keV, respectively.

2.4.1. Experimental Setup

A schematic representation of the experimental setup, shown in Figure 2.13, was built at the beamline and reported in Castoldi *et. al* (2007). A laminar beam was used for imaging the sample by adjusting the tungsten-slit system located at the entrance of the experimental hutch. The laminar beam was 500 µm thick for diffraction images and 5 mm thick for transmission images. The CDD was mounted on a goniometric cradle used to tilt the system at 9 degrees, with respect to the original beam direction, in order to acquire diffraction images. A multi-hole brass collimator (shown in the schematic in Figure 2.13b), with 500 µm x 500 µm hole size and 500 µm spacing between holes, was mounted in front of the detector to gather the scattered photons for diffraction imaging. Diffraction and transmission images of the samples were acquired with the CDD.

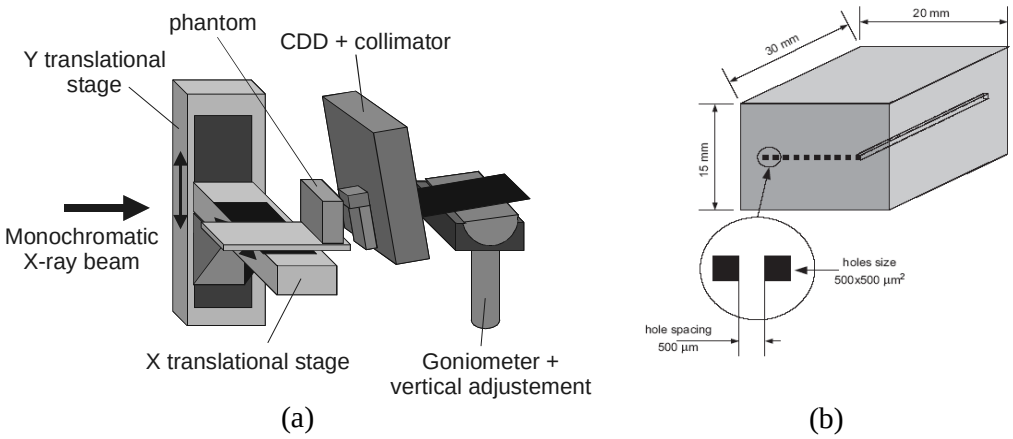

Figure 2.13: Schematic drawing of (a) the setup mounted at the SYRMEP beam-line to evaluate the performances of the CDD in DEBI measurements (Castoldi *et. al.* 2007) (b) the multi-hole brass collimator used in diffraction imaging (Vedani, 2007).

Transmission images were acquired without the multi-hole collimator and with the detector surface set orthogonal to the beam direction. “Diffraction images were acquired with the detector-collimator system by vertically scanning the sample in front of the beam. For each vertical position of the sample, two images, with a 500

µm horizontal displacement of the sample, were acquired, in order to cover the whole sample area which was obscured by the spacing between the collimator holes"(Castoldi *et. al.*, 2007).

2.4.2. Data Acquisition

The signals from the detector's channels are amplified by the preamplifiers, and filtered by the shaper in the analog front-end while the digital back-end digitizes the signal waveforms with fast ADCs as well as it stores and subtracts the background waveform from the signal waveforms. The acquired signal waveforms are then searched for pulses and, if found, the samples around the peaks are sent via the Versa Module Eurocard (VME) bus and Peripheral Component Interconnect (PCI) bridge to the host PC, where amplitude and time centroid of each detected pulse are computed and stored (Galimberti, 2004).A C++ based acquisition software monitors the acquired data remotely. A block scheme of the read-out chain is shown below.

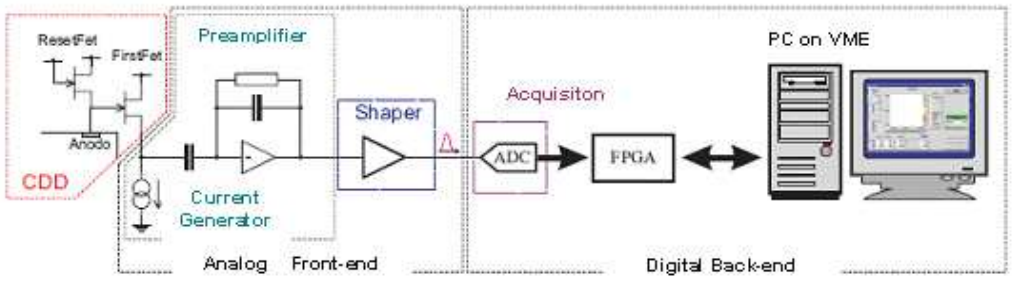

Figure 2.14: Block scheme of the read-out electronics. The analog front-end amplifies and filters the signal while the digital back-end acquires and subtracts the background and makes the amplitude and time measurements (adapted from Galimberti, 2004).

2.4.3. Energy Spectrum of the Synchrotron Beam

The beam spectrum was measured with the detector set both for transmission image

acquisition and for diffraction image acquisition, is shown in Figure 2.15. For the transmission spectrum, nothing was placed between beam and detector. For the diffraction spectrum a collimator was mounted in front of the detector to gather the scattered photons from the scatterer placed in front of the detector-collimator system, which was set at the diffraction angle of 9 degrees. The energy of the beam was set to 18 keV.

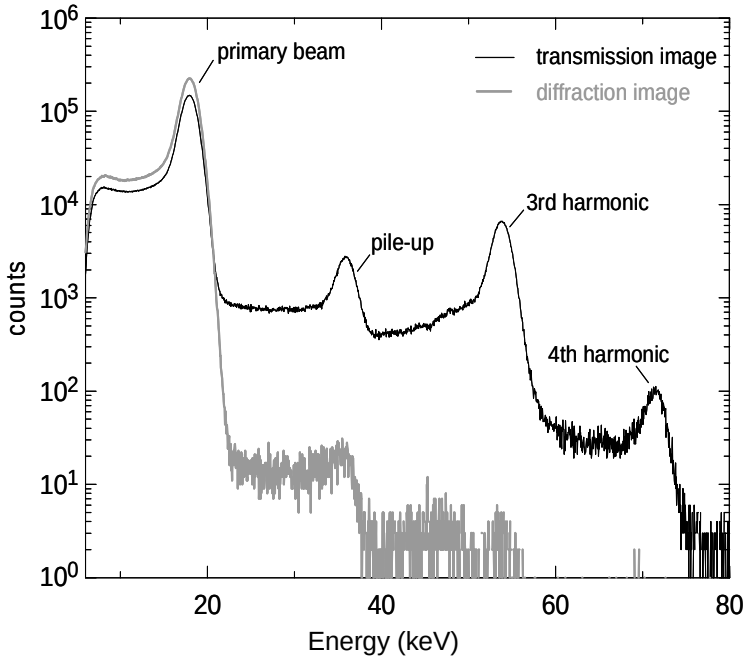

Figure 2.15: Measured spectrum with the detector set both for transmission images acquisition and for diffraction images acquisition. The energy was set to 18keV(Castoldi *et. al.*, 2007).

The monochromator crystal, Si(111), at the beam line is used to set the energy of the beam. The crystal not only transmits the desired fundamental energy which is 18 keV, but also the third and fourth harmonics. The allowed harmonics for Si(111) include (333) and (444) and the peak located at twice the desired energy (36 keV)is due to the pulse pile-up in the detector (Castoldi *et. al.*, 2007). The beam intensity was not corrected for either spectrum so the diffraction spectrum has a higher

intensity at 18 keV than the transmission one.

2.4.4. Samples for Transmission and Diffraction Imaging

There were two sets of samples imaged for this experiment, namely, the phantom and tissue samples. The phantom was a Perspex© slab with 3 holes of different diameters drilled in it, used for preliminary testing.

In order to better assess the performance of the Controlled-Drift Detector in DEBI measurements, two tissue samples (Pork muscle with regions of fat) were analyzed. The first tissue sample, which is shown in the photograph in figure 2.16a (Castoldi *et. al.,* 2007), was about 5 mm thick. The thickness of the sample was chosen to be larger than the depth (i.e. along the beam) of the voxel (500 μm / sin(θ)=3.2 mm). This sample was selected for having two distinct regions of muscle and of fat, which feature scattering properties very close to those of tumor and of normal breast tissue respectively[*].The second meat sample, as seen in the photograph in figure 2.16b from the same publication, was chosen due to its smaller and more complex fat structure nested in the muscle tissue with details less than 1 mm in size.

(a) (b)

Figure 2.16: Photographs of the (a) first analysed tissue sample (Tissue 1), (b) second analysed tissue sample (Tissue 2), taken from (Castoldi *et. al.*, 2007), with the imaged areas marked.

[*] This information was provided by Professor G. Royle of UCL (UK), verbally

2.4.5. Preliminary Assessment of Images

The preliminary construction of the images resulted in a 0.29 contrast between fat and muscle for the transmission image of the first tissue sample at 18 keV and 0.12 for the transmission image at 26 keV. The contrast for the diffraction images was 0.48 and 0.30 at 18 keV and 26 keV, respectively.

The contrast in transmission images, between fat and muscle for the second tissue sample, was 0.33 and 0.11 at 18 keV and 26 keV, respectively. In the case of diffraction images it was 0.46 and 0.29 at 18 keV and 26 keV, respectively. All these values are given in Table 1 below

Table 1. Contrast Comparison of the tissue samples from Transmission and Diffraction imaging at beam energies, 18 keV and 26 keV (Castoldi *et. al.*, 2007).

Meat Sample	Energy	Transmission image	Diffraction image
First	18 keV	0.29±0.02	0.48±0.03
First	26 keV	0.12±0.01	0.30±0.03
Second	18 keV	0.33±0.03	0.46±0.05
Second	26 keV	0.11± 0.01	0.29±0.02

CHAPTER 3

MATERIAL AND METHOD

This study is based on a detailed analysis of the data obtained from the images produced as a result of an experiment conducted under the supervision of Dr. Castoldi and Dr. Guazzoni of Politecnico di Milano and Dr. Royle of University College London, in the year 2005 at the SYRMEP beam-line at the ELETTRA synchrotron in Trieste (Italy). Details of this experiment are given in section 2.3 of this thesis. The preliminary results of this data can also be found in Castoldi *et. al.* (2007).

The performance of the CDD, details of which are given in section 2.2.2, was assessed on the basis of the data on the measurements of diffraction enhanced imaging of the phantom and pork tissue samples. The material and method employed in this study are presented in the following sections.

3.1. Analysis Material

The following material was used to assess/diagnose the performance of the detector:

i. The data obtained from the DEI experiment held at ELETTRA which was stored as binary files on a disk
ii. Data included each detected event which consisted of two variables, i.e. the amplitude of each signal in Volts and the drift time in seconds. An event is considered to be the photon that reaches the detector and a signal is considered to be the amount of ionized charge readout at the anode

iii. In-house MATLAB© macros were used to perform the final data calibration for the energy and interaction coordinate
iv. New set of routines developed, in MATLAB©, by the author for the reconstruction of the final X-ray images
v. A desktop computer (Windows 2000 OS) for processing the data files
vi. Contrast values between two materials (pork fat versus muscle) of the tissue samples in the preliminary transmission and diffraction images taken from Castoldi *et. al.* (2007)

3.2. Analysis Method

The following steps were followed to assess the detector's performance and to reproduce the transmission and diffraction images of the samples:

i. MATLAB© macros were used to study the different type of detected events and perform the final data calibration for the energy and interaction coordinate
ii. Data from the binary files pertaining only to the beam was used to calibrate for energy and time. Calibration refers to the analysis of the data where energy and time of the events are determined and not the detector itself.
iii. Energy calibration coefficients were used to determine the energy of each event gathered from imaging the samples
iv. Once energy of each event is determined, energy time windowing is done to exclude unwanted events
v. Time calibration was used to locate the interaction coordinate of each event
vi. Routines developed by the author were used to create image frames using the time and energy calibration. A frame is the image acquired after the sample/detector linear stages have completed a given position. Each frame was created with the relevant energy cut imposed on it.
vii. Reconstructing transmission and diffraction images using the calibrated frames and the file containing the linear stage position at each frame acquisition. Routine corrects for beam intensity and divides by flat-field

image for both transmission and diffraction images. The counts in each collimator hole are summed in order to create “new pixels” for reconstructing diffraction images

viii. Contrast values between two materials of the tissue samples from the transmission and diffraction images were compared to the contrast values cited in literature, to assess the applicability of the detector to this technique

Details pertaining to the data calibration and analysis are given in the following chapter.

CHAPTER 4

DATA ANALYSIS AND RESULTS

The data obtained from the DEI experiment held at ELETTRA was stored on a disk. This data included information concerning each detected event, i.e. the amplitude of each signal in Volts and the drift time in seconds.

MATLAB© macros were developed in-house for calibrating and analyzing this data. The data calibration was done using the data collected by irradiating the detector surface with the synchrotron beam. Energy calibration coefficients were used to determine the energy of each event gathered from imaging the samples and the time calibration was used to locate the pixel each event belonged to. These energy and time calibration values were then used to analyze the behavior of the beam and the detector, and reconstruct the transmission and diffraction images of the samples. The procedure for obtaining these calibration values are discussed in the next section.

4.1. Detector Performance and Calibration

All of the detector channels have the on-chip Reset FET and has the deep n implants called channel guides. Preliminary to the experiment the detector was irradiated with a ^{241}Am source in order to test and compare the performance of the detector channels with the channel guides of different thicknesses.

Shown in Figure 4.1 is a scatter plot of the events gathered in channel 3 of the detector. There is a decrease in the amplitude along the pixels which is clearly seen in the 60 keV line of the ^{241}Am source. The amplitude is reduced from 0.96 V in

pixel 1 to 0.84 V in pixel 34. This reduction in amplitude increases for each pixel located further away from the readout anode and is a result of the broadening of the charge cloud due to the Coulomb repulsion and thermal diffusion. The widening of the cloud depends on the time it takes the charge packet to reach the anode, growing therefore with the distance of the pixel from the anode and to the decrease in the drift field which is dependant on the biasing of the detector.

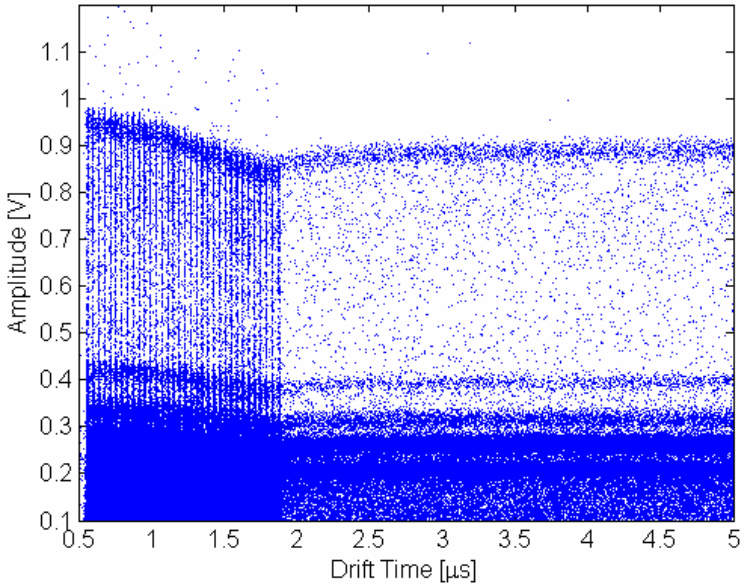

Figure 4.1: Scatter plot amplitude vs. drift time of events gathered from a single detector channel (Channel 3) with the ^{241}Am source irradiating the detector.

The ideal signal is that of a delta-like signal charge at the anode but during the drift the charge cloud expands. As a first approximation, neglecting the electrostatic repulsion and assuming the diffusion alone means that the delta-like charge packet attains a Gaussian shape by the end of its drift. The variance of the signal can be expressed in terms of diffusion,

$$\sigma_x = \sqrt{2D_n T_{dr}} \tag{5.1}$$

where D_n is the diffusion coefficient of the electrons in silicon, estimated considering a mobility of 1400 cm^2 /(V s), and T_{dr} is the total drift time. At the anode this charge is converted to a current signal which is a Gaussian pulse with a standard deviation of:

$$\sigma_D = \frac{\sqrt{2D_n T_{dr}}}{v_d} \tag{5.2}$$

where v_d is the drift velocity. The resultant signal at the output of the shaper is a convolution of the ideal shape and the Gaussian charge pulse and retain the Gaussian shape but with lower amplitudes. The amplitude is given by:

$$\frac{A}{A_0} = \frac{\sigma_{sh}}{\sqrt{\sigma_{sh} + \sigma_D}} \tag{5.3}$$

where σ_{sh} is the shaping time of the shaper, A is the amplitude of the signal immediately after its diffusion, while A_0 is the ideal amplitude of the signal. These effects degrade the charge resolution, in particular for the last pixel in the drift column due to its longer drift time and hence greater charge diffusion with respect to the first pixel. This is called ballistic deficit.

In the case of Channel 3 (Figure 4.1), using equation 5.3 would give a reduction of 2%. However, experimental data, instead, shows that the reduction between the first and the last pixel is about 12.5%. These results show that there is a relatively strong non-linear behaviour of the FET that causes the marked reduction of the amplitude along the pixels

For the purpose of testing the effect of the channel guides, different thicknesses of were implanted in certain channels. The 22 channels of the detector can be bunched according to these differences in their designs. Channels 3 and 4 have the 60 μm, channels 5 and 6 have the 50 μm, channels 7 and 8 have the 40 μm and channels 9 to 22 have the 30 μm thick deep n implants.

Shown in Figure 4.2a is a plot of the average time difference between the pixels for each channel and Figure 4.2b shows the average time resolution of the pixels of each

channel. The discrepancy in the time difference and the temporal resolution is to the order of 1 ns.

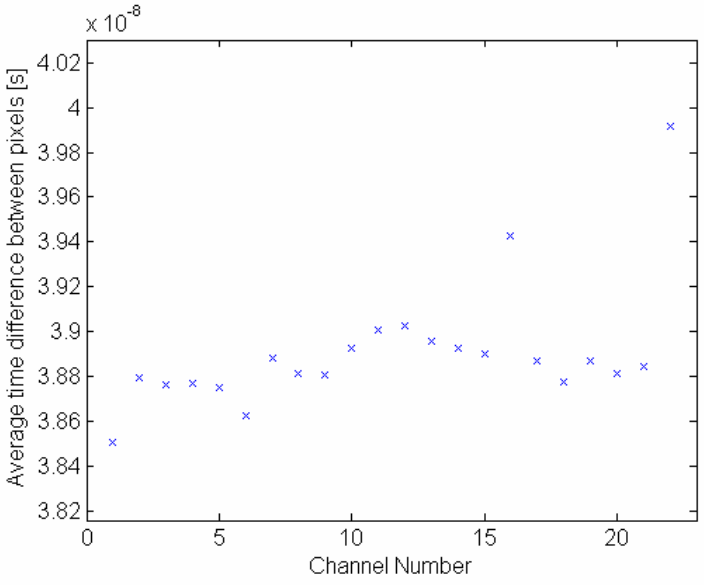

(a)

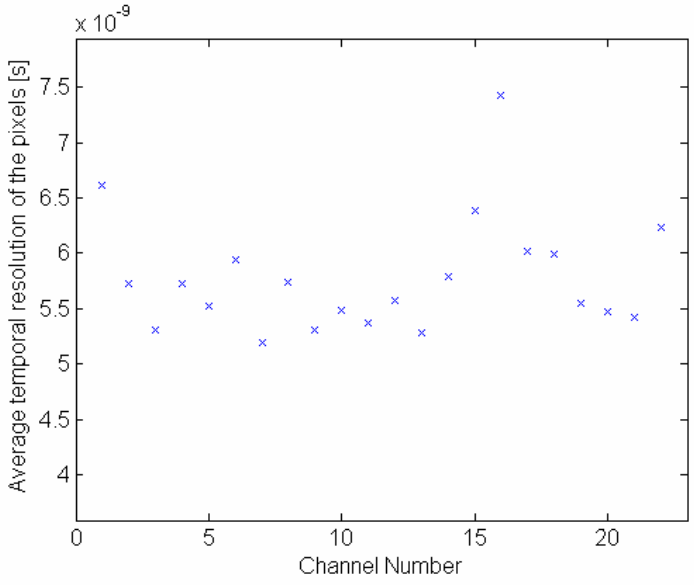

(b)

Figure 4.2: (a) Plot showing the average distance between pixels for every channel and (b) Plot showing the temporal resolution of the pixels for every channel, in order to compare the performances of the channels with different deep n implant widths.

Channel 16 has dead pixels so the average was computed disregarding the time difference between the pixel right before and right after the dead area. However it can be clearly seen that the different groups of channel do not show differences between eachother.

a) Detector Calibration

The synchrotron beam was used to calibrate the detector. The data was collected with the detector in transmission mode and without any sample in front of it. The Amplitude versus Drift time scatter plot - shown in Figure 4.3a for a single channel of the detector - provides, besides calibration, a precise tool to analyze/diagnose detector features and performance.

The events are mostly gathered in clusters around certain amplitude values and the drift time of the pixels as shown in area (1), in Figure 4.3b. These are the events which will be attributed to the right energy and position. However, there are other groups of events too.

Area (2) shows the events which seem to have higher amplitudes than the incoming beam. When two photons are collected in the same column in the same integration phase their charges are read out as a superposition of the two signals due to the single charge packets. This is effect is called pile-up.

Area (3) shows the charge sharing of the photo-generated charge that takes place between two adjacent pixels in different drift columns. The charge collected in each single column is a fraction of the initial photo-generated charge, hence giving a lower amplitude value with respect to the initial photon energy. If charge sharing happens between two adjacent pixels in the same drift column, the anode collects the total charge. As the time difference between two adjacent pixels is much shorter than the typical pulse duration, the measured amplitude is the sum of the partial charges in the two pixels. The measured amplitude remains the same as the total charge but with drift time values intermediate to those of the two pixels. This effect is called inter-pixel charge sharing and is shown in area (4).

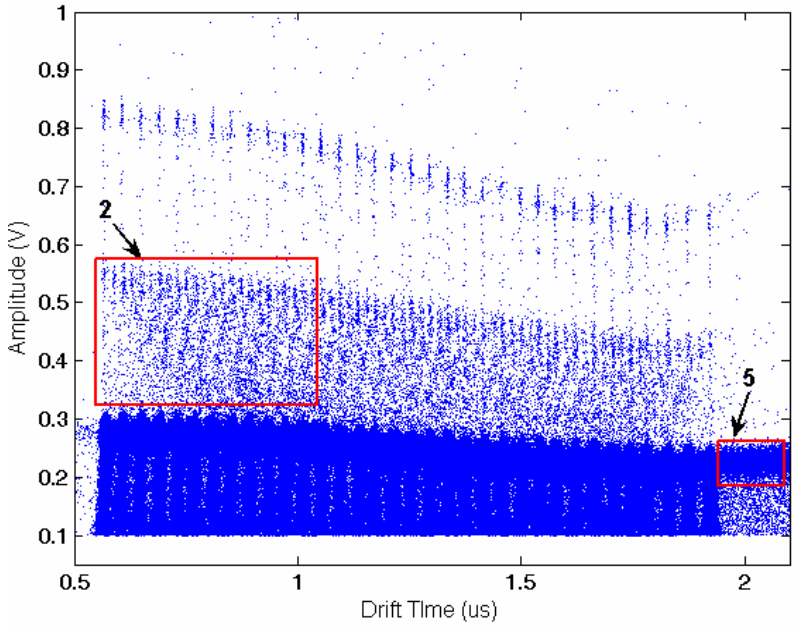

(a)

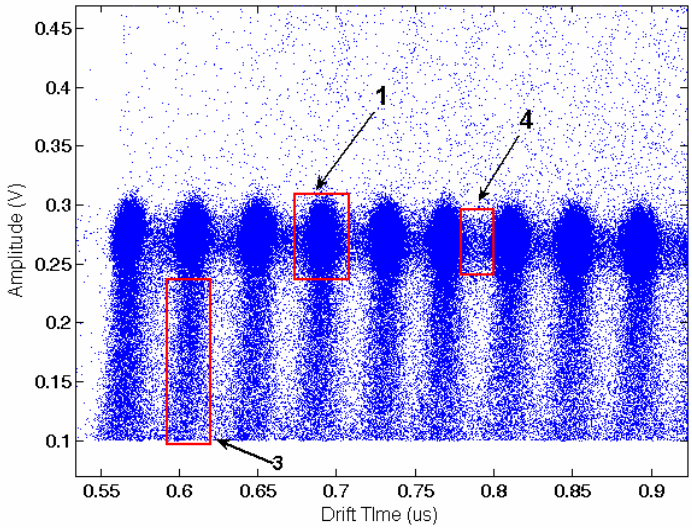

(b)

Figure 4.3: (a) Scatter plot amplitude vs. drift time of the synchrotron X-rays at 18 keV, collected from one of the detector channels. Groups of events shown in areas (2) and (4) are due to pile up and inter-pixel charge sharing, respectively. (b) A close up of some of the pixels shows area (1) shows the correctly detected photons in a pixel, (3) with charge sharing in a drift column and (5) shows the out-of-time events.

Area (5) shows the so-called "out-of-time" events. These are events that hit the detector during the readout phase and not during the integration phase. As the

interaction time of these events is random, their measured drift time will be uniformly distributed on the time axis. Photons hitting the detector during the transport of the integrated charges (corresponding in Figure 4.4a to the time window 0.6 μs-1.9 μs) will therefore appear both in area (1) and (4). Area (5) clearly shows the photons hitting the detector after the collection of the integrated charges, before the new integration phase is re-started.

This result is also corroborated from the work reported in Castoldi *et. al.* (2002).

From the scatter plot shown in Figure 4.3a, one can obtain the energy distribution and the drift times of each pixel of each channel for 2D localization of the signal events.

The time calibration is done using the temporal distribution of the drift times measured by each detector channel. The events are binned along the drift time axis. A minimum count threshold is set and three time windows (on the order of 1ns) are determined in order to find the number of pixels and make an approximate localization of the pixel maxima. This is done by comparing the sum of the counts between the three windows as they move along the binned axis.

Once the pixels are found a minimum and maximum limit around each pixel is set by taking half the time difference between adjacent pixels. Then a Gaussian fit is imposed encapsulating the events that fall between these limits. In this way the centroid, the area and the standard deviation of each pixel is determined. The events in a channel are placed in to the appropriate pixel according to their maximum and minimum drift time limits, during image reconstruction.

In this way, the distribution of the events along the time axis gives one of the two position coordinates. The second is obtained from the granularity of the anodes.

The average temporal distance between the pixels is 40 ns and the average temporal resolution is 6 ns FWHM for the distribution shown in Figure 4.4. The former is related to the drift velocity, the latter depends on readout noise and the photon energy.

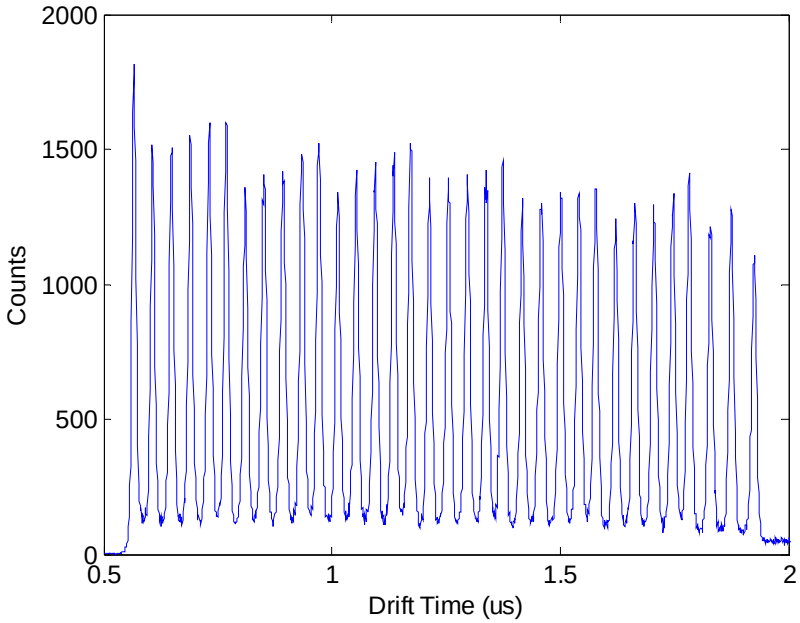

Figure 4.4: Distribution of the events along the time axis, obtained from the scatter plot of a single detector channel, gives one of the 2D positions.

The energy calibration can be obtained from the scatter plot (e.g. Figure 4.3a), looking at the energy distribution collected by every pixel, when irradiating the detector with a known radiation source.

Normally, after binning the amplitude axis, each peak in the individual pixel spectra is fitted with a Gaussian. The centroid of each fit is then assigned to its known energy value. Linear regression conveys the energy calibration factors of the detector.

The energy calibration can then be used to understand the nature of events gathered during acquisition and also window on the desired energy range for reconstructing and analyzing images.

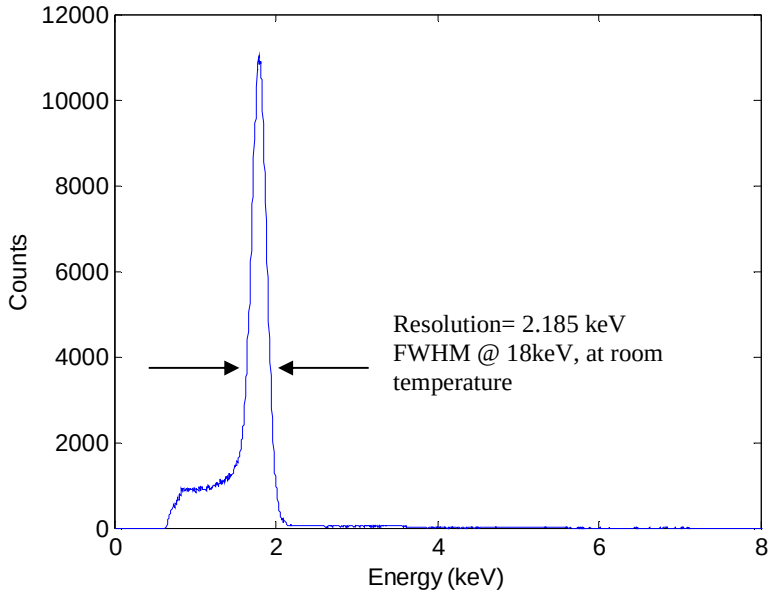

Figure 4.5: The energy spectrum from a single channel (channel 10), acquired by irradiating the detector with the synchrotron beam at 18 keV. The amplitude of the events are readout in Volts and with a simple fitting procedure applied to each pixel, the energy of each event is found. The energy resolution is 2.185 keV FWHM, at room temperature.

The measured energy resolution was about 2.185 keV FWHM at 18 keV synchrotron beam energy, at room temperature. The measured resolution was relatively high (compared with values reported in section 2.2.2.4) due to an excessive leakage of the detector prototype used in this experiment.

Shown in Figure 4.6 are the scatter plots demonstrating the detector's stability through out time. Figure 4.6a shows the Energy versus Absolute time while Figure 4.6b shows the Drift Time versus Absolute time. Absolute time is a form of 24 bit integer counter that helps keep track of the number of events saved.

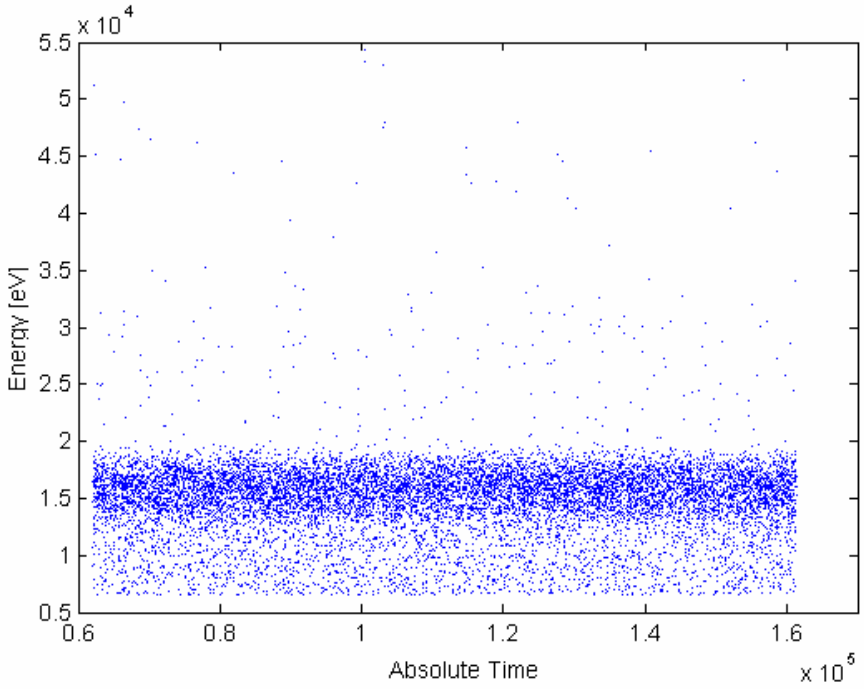

(a)

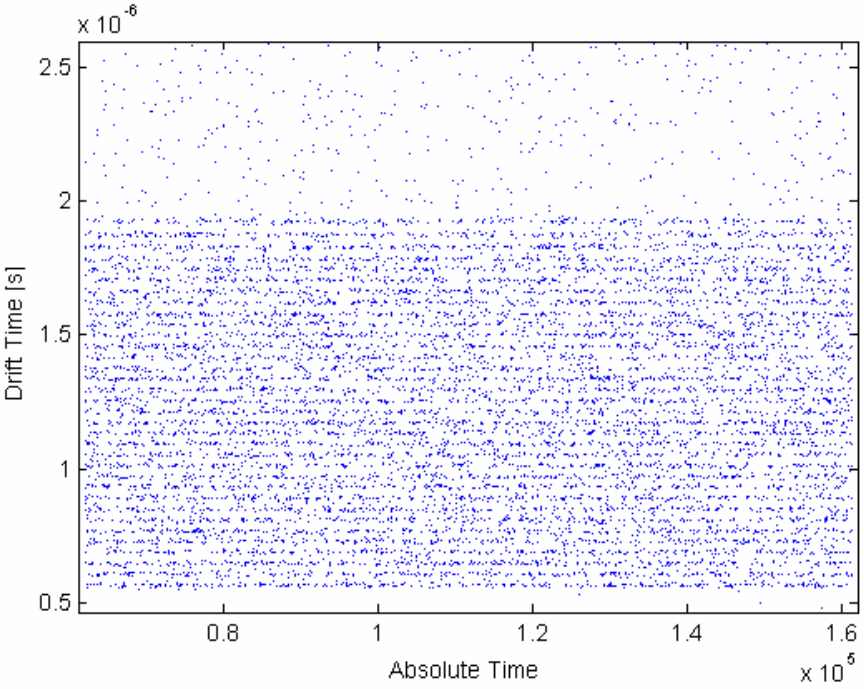

(b)

Figure 4.6: (a) Plot of Energy versus absolute time (24-bit counter of events saved) and (b) Drift Time of all 34 pixels versus absolute time relevant to the channel 3 of the detector. These two plots agree with the reconstruction of eventual motion of the sources.

Both energy and the drift times of channel 3 are stable through out the acquisition. These two graphs are in agreement and it is possible to perform a sequential reconstruction of the recorded events. This type of a stability check allows us to follow the evolution of time-varying sources also. The images presented in this work are all static; however there is no variation in the peak of the source.

4.2. Imaging of Phantoms

Transmission images were acquired with the collimator removed and the detector set orthogonal to the primary beam. Figure 4.7 shows the beam profile with the detector in transmission mode. Such an image, generally called the *flat- fıeld image,* is used to normalize the acquired transmission images in order to account for the non-uniformities of the beam and detector response. Along the pixels an impression of the p-side strips can be seen clearly. The top most row (Channel 1) and pixels 8-11 on channel 16 are dead. Channel 2 has more counts on it due to the beam having a higher number of counts in that region.

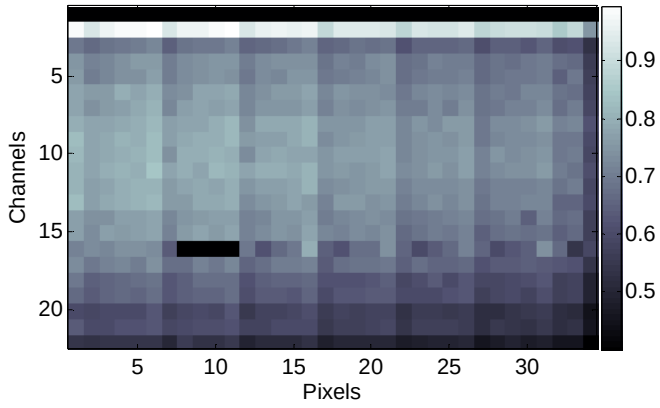

Figure 4.7: Image of the synchrotron beam with the detector in Transmission mode. The top most row (Channel 1) and pixels 8-11 on channel 16 are dead.

Diffraction images were acquired with the mechanical collimator mounted in front of the detector and the detector-collimator system placed at a 9 degree scattering angle. An image of the collimator with the detector in diffraction mode can be seen in Figure 4.8. Only one row of holes was used for image reconstruction. The images were acquired by vertically scanning the sample in front of the beam. For each vertical position, two images, with a 500 µm horizontal displacement of the sample, were acquired, in order to cover the whole sample area for two beam energies. This procedure was repeated at two beam energies. For diffraction images the flat-field image was obtained with a uniform scatterer in front of the detector, instead of the sample, in diffraction mode.

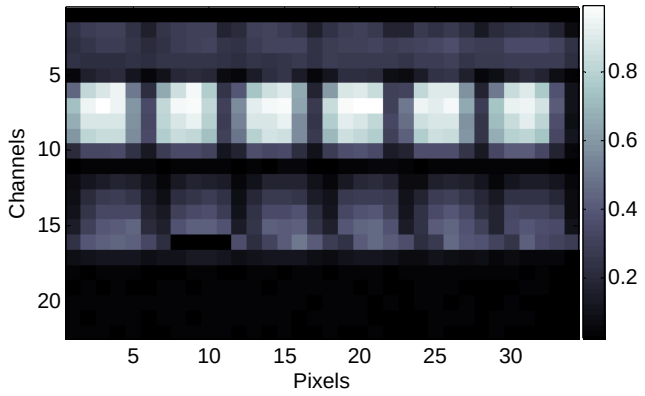

Figure 4.8: Image of the mechanical collimator, mounted in front of the detector, with the detector in Diffraction mode. A uniform scatterer was placed instead of the sample to obtain a flat image. Only a single column of holes was used for imaging. The loss of data due to the spacing between the holes was recovered by moving the sample horizontally by 500 µm.

The first sample to be imaged was the phantom of 5 mm thick Perspex with holes of 4, 2 and 1mm diameter. Figure 4.9a shows the transmission image acquired at 18 keV and reconstructed. The bright areas (corresponding to a higher exposure) in the transmission image in Figure 4.9a are the holes.

The sample linear stages were used to step at specified positions in order to image a

sample completely. At the completion of each step an image frame was acquired. The detected events in each image frame were calibrated for energy and interaction position. The required energy windowing is done during the creation of the frames by considering the events in each pixel of each channel that fall within the limits imposed. All image frames are corrected for beam-intensity and detector-response non-uniformity by means of a flat-field image. The flat-field image is also windowed in the desired energy range before normalization. Using the sample stage positions and the calibrated frames, a final image of the object is reconstructed.

Figure 4.9b shows the diffraction image acquired at 18 keV of the Perspex phantom. The bright areas that correspond to a higher exposure in the transmission image are the holes, which now appear darker (thus representing a lower exposure) in the diffraction image due to the lower scattered intensity from air with respect to Perspex.

For each detector pixel, the counts within an energy window of 5 keV centered at the photo-peak energy were selected. All pixel counts corresponding to the same collimator hole were summed; hence, each line of a diffraction image consisted of 12 pixels 500 µm × 500 µm in size. The images were normalized to their maximum count to impose the same color scale on the images. The scale range is then 0 – 1 and helps in comparing the two images with each other.

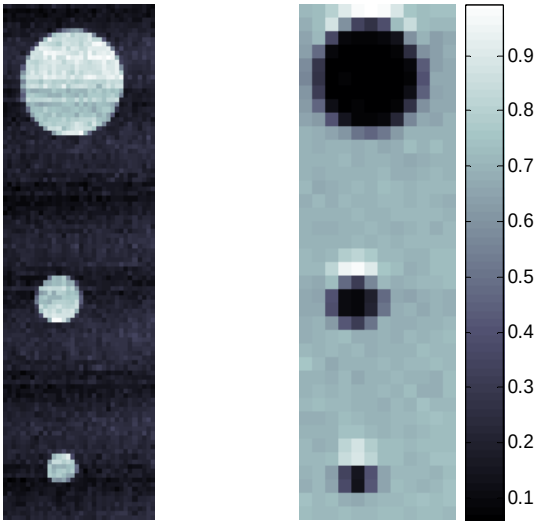

(a) (b)

Figure 4.9: Transmission and diffraction images of the Perspex phantom at 18 keV. (a) Transmission image – empty holes. (b) Diffraction image – empty holes along with the color scale of the normalized images.

4.3. Imaging of Tissues

In order to better assess the performance of the Controlled-Drift Detector in diffraction enhanced imaging of tissues, two pork samples were analyzed. The tissue sample shown in Figure 2.16a was selected for having two distinct regions of muscle (the dark area in the transmission image) and of fat (the bright area in the transmission image). Figure 4.10a shows the transmission image of this sample at 18 keV and Figure 4.10b shows the diffraction image at the same energy. Figures 4.10c and 4.10d show the transmission and diffraction images at 26 keV, respectively. The diffraction images were slightly misaligned with respect to the transmission ones.

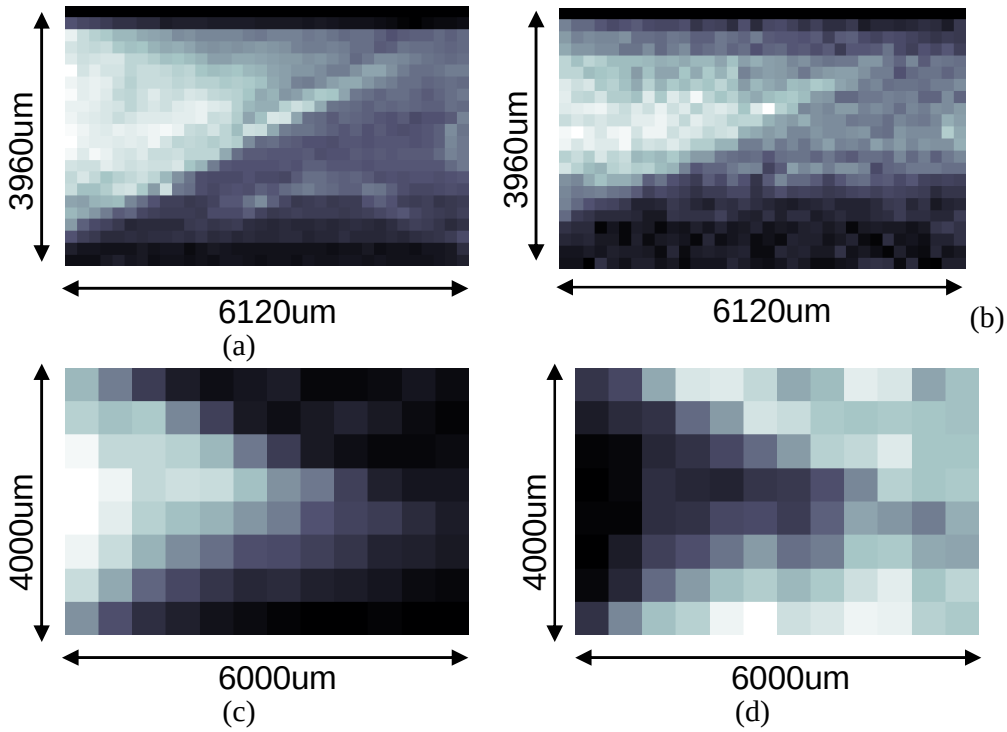

Figure 4.10: (a) Transmission image at 18 keV. (b) Diffraction image at 18 keV. (c) Transmission image at 26 keV. (d) Diffraction image at 26 keV. Images were normalized by their respective flat images.

The transmission and diffraction images of the tissue samples, along with their flat-field images were windowed in the 5 keV range around the photo-peak in order to neglect the effects of pile-up in the detector and the higher harmonics due to the monochromator crystal at the synchrotron. The images have been normalized with their respective flat-field images.

The contrast between muscle and fat in the two diffraction images is reversed as expected, since fat diffracts more than muscle at χ=1.1 nm^{-1}, while the opposite occurs at χ=1.7 nm^{-1}. Although the measurement was limited to two values off the momentum transfer, this demonstrates the sensitivity to tissue type by appropriate choice of momentum transfer.

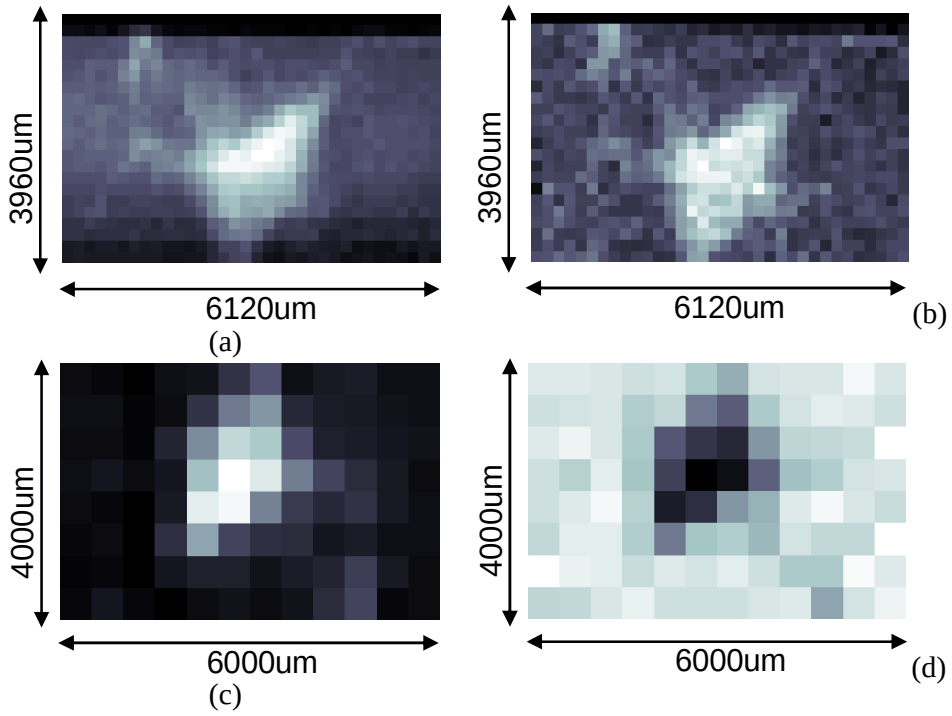

Figure 4.11:(a) Transmission image at 18 keV. (b) Diffraction image at 18 keV. (c) Transmission image at 26 keV. (d) Diffraction image at 26 keV. Images were normalized by their respective flat images.

As mentioned in section 2.3.4 a second tissue sample was also imaged since it presented a fat structure with details less than 1mm in size. Figure 4.11b and 4.11c show the transmission and diffraction images of this sample at 18 keV, while Figure 4.11d and 4.11e show the transmission and diffraction images at 26 keV, respectively.

The diffraction images were slightly misaligned with respect to the transmission ones in this case, too. The same behavior as the previous sample was obtained where, fat regions are clearly distinguished from muscle ones in the diffraction images.

The measured contrast between the two materials between the two tissues (i.e. fat and muscle) for the samples in the transmission and diffraction images is summarized in Table 2 below.

Table 2. Contrast Comparison of the tissue samples from the Transmission and Diffraction imaging at beam energies, 18 keV and 26 keV (from Figures 4.8 and 4.9).

Sample	**Transmission (18 keV)**	**Diffraction (18 keV)**	**Transmission (26 keV)**	**Diffraction (26 keV)**
Tissue 1	0.33±0.02	0.51±0.03	0.13±0.02	0.48±0.03
Tissue 2	0.43±0.02	0.49±0.05	0.11±0.03	0.30±0.02

These contrast values are close to those mentioned in Table 1 from section 2.3.5, which were taken from Castoldi *et. al.* (2007). Of the eight contrast values, only two are different: diffraction contrast for Tissue 1 at 26 keV and both transmission and diffraction for Tissue 2 at 26 keV. These differences may be due to the method of calculating the contrast. An area was determined (2x2 pixels for diffraction images and 3x3 for transmission images) in each material to calculate the contrast, while in Castoldi *et. al.* (2007) the calculation was done by choosing a single pixel in each material. The contrast was calculated by taking the ratio of the difference of the counts to the sum of the counts in the two materials.

A bicubic interpolation algorithm was carried out for the preliminary construction of the final images by the experimentalists. There has been no interpolation imposed for the reconstruction carried out by the author.

It can be seen from the diffraction images of the samples that the spatial resolution is very poor compared to the transmission images. This is due to the multi-hole collimator used for these tests. The size of single hole is 500 µm, which drastically reduces the image quality. It should, however, be noted that DEI is not intended to replace but to accompany transmission images, by increasing contrast and providing tissue discrimination.

CHAPTER 5

CONCLUSIONS

Diffraction Enhanced Imaging (DEI) is a technique developed to improve the diagnostic capabilities of radiography. The main limitations of standard DEI setups stem from the detection system and from the requirement of the synchrotron source.

An X-ray imager that would allow efficient detection was required to tackle with the limitations of the technique and the experimental setup. For this reason, the detector in the synchrotron setup was upgraded to a novel single-photon counting 2D X-ray imager with spectroscopic capability at high frame rates; namely, the Controlled-Drift Detector.

An analysis of the X-ray images taken at ELETTRA with the CDD, has been carried out for detector qualification purpose. A study of the different types of detected events and the final data calibration for the energy and interaction coordinate, using the drift times, was performed.

All the channels of the detector have the Reset FET at their readout. A relatively strong non linear behaviour of the FET was observed, which causes the marked reduction of amplitude along the pixels. In order to reduce this effect of ballistic deficit the removal of the Reset FET is considered for future prototypes of the detector.

There are different types of topologies used in the detector design where the channels can be divided into four groups according to the widths of their deep n implants. The 30 μm wide channel guide performs just as well as the other channel guides and so, it

can be implemented in all channels in future prototypes. There is very little sensitivity of the drift velocity to wider implants.

By looking at the distribution of events according to their energy and drift time throughout the acquisition shows the stability of the detector as the source (synchrotron beam) was not varying in time in either energy or position.

By studying the time distributions of the pixels it can be seen that they are well separated despite the high leakage current, which guarantees good position sensing capability. The temporal distance between the pixels and the temporal resolution in the case of both types of channel are equivalent. The drift velocities are also equal which shows the consistency of the performance of the channels.

In the study of the events gathered from the synchrotron beam it was noted that higher harmonics were also present, which in turn can cause degradation in the image quality. As a result of the energy discrimination of each detected photon, the CDD allows understanding events and phenomena which would not be explicit with the employment of conventional 2D X-ray imagers. The ability to chose the energy range of interest enables constructing images by neglecting the added contribution from unwanted events.

Also noted were the pile-up events which are specific to the detection system. The energy resolution of the detector prototype used in the experiment is 2.185keV, due to high leakage current however, better energy resolution of an order of magnitude are typically achievable in selected prototypes. Cooling the detector by few degrees will help eliminate leakage current and achieve a better resolution.

A new set of routines have been developed in MATLAB© which take into account all the required normalizations (flat field image, beam current, background) and energy windowing for the reconstruction of the final X-ray transmission and diffraction images. The final outcome is a user-friendly and dedicated data analysis system suited for this type of detector and experiment.

The values of image contrast extracted with these routines (Table 2) are in good agreement with the values obtained by the experimentalists.

It can be seen from the reconstructed diffraction images that the spatial resolution of the diffraction images is poor compared to the transmission images. This is due to the limited spatial resolution of mechanical collimator system. The use of collimators is necessary to gather the scattered X-rays however; the mechanical multi-hole collimator introduces a drawback. It limits the achievable spatial resolution due to the mechanically conceivable hole size/spacing and requires increasing the acquisition time due to the duty cycle of hole versus spacing. Hence, it only gives an idea about the location of a material but not a one-to-one correspondence with the transmission image.

New developments in polycapillary X-ray optics technology enable the upgrade of the DEI setup. In order to handle the limitations due to the collimation a polycapillary lens can be coupled to the detector. As the diameter of a single capillary can be as small as few micrometers, by matching the capillary size to the detector pixel the full spatial resolution of the detector can be exploited. Study of such a lens collimator is being carried out at present using polychromatic source and constitutes one relevant perspective of this work.

The results presented in the previous chapter encourage pursuing the application of CDD to DEI. The energy discrimination quality of the CDD allows the possibility of investigating several energy windows or momentum transfer values, in order to achieve a better identification in tumor detection.

Presented is a recommendation to further the multi-momentum transfer analysis. The synchrotron radiation DEI setup based on scatter selection allows the acquisition of images at specific momentum transfer values by either changing the beam energy or the diffraction angle. In the setup at ELETTRA, the diffraction angle was kept fixed while the beam energy was changed. An image of the sample was acquired at different energies. At each energy of the beam, the contrast of the materials in the sample either increase or decrease in contrast, one respect to the other, according to their linear scatter coefficient distribution in energy.

By looking at the behaviour of the counts gathered in a single voxel, at each beam energy, it is possible to reconstruct a distribution proportional to the linear scatter

coefficient distribution with respect to the momentum transfer or energy of the materials. This may further help in the investigation of the material constituents of the sample and the weight fraction of a constituent material in each voxel.

The calculated linear differential scatter distributions can be compared with those of the standards in literature in order to make a better assessment about the validity of the distribution or the possibility of the existence of other materials.

This type of a multi-momentum reconstruction can be greatly eased with the employment of a Controlled-Drift Detector. Due to its energy windowing capability a polychromatic source may be used instead of the synchrotron beam while keeping the angle of the detector collimator system at a fixed diffraction angle. In this way a single image is enough for re-creating the possible linear scatter distribution and extracting the weight fractions of the materials in a single voxel of the sample.

The ability to use a conventional X-ray generator allows a great advantage in the possible translation of a transmission and diffraction imaging setup from the synchrotron to the clinic.

It should be noted that DEI is not a technique intended to replace conventional transmission imaging techniques. It was intended that DEI should accompany the images of samples obtained from conventional transmission imaging, by increasing contrast and hence, providing material discrimination. This is because the technique has a strict limitation on the yield of scattered photons since the probability of scattering is very low. A second limitation, as mentioned above, is the limit on the spatial resolution of the diffraction images placed by the multi-hole collimator and hence the visual distribution of materials.

REFERENCES

Castoldi A., Rehak P., *High charge effects in silicon drift detectors with lateral confinement of electrons*, IEEE Nucl. Sci. Symp. and Med. Imag. Conf. Rec. vol. 1, pp 588-591, 1995.

Castoldi A., Rehak P., Holl P., *A new silicon drift detector with reduced lateral diffusion*, Nucl. Instr. and Meth. A377, pp. 375-380, 1996.

Castoldi A., Guazzoni C., Longoni A., Gatti E., Rehak P., and Strüder L., *Conception and Design Criteria of a Novel Silicon Device for the Measurement of Position and Energy of X-Rays*, IEEE Trans. Nucl. Science 44, 1724-1732, 1997a.

Castoldi A., Rehak P., Holl P., *Signal charge sharing in multilinear drift detectors: design and experimental characterization*, IEEE Trans. Nucl. Sci., vol. 44(2), pp 131-144, 1997b.

Castoldi A., Gatti E., Guazzoni C., Longoni A., Rehak P., Strüder L., *The controlled-drift detector: characterisation of the readout mechanism and of the charge handling capability*, IEEE Nucl. Sci. Symp., Conf. Rec., vol. 1, pp 138-141, 1998.

Castoldi A., Gatti E., Guazzoni C., Longoni A., Rehak P., Strüder L., *Analysis and characterisation of the confining mechanism of the controlled-drift detector*, IEEE Trans. Nucl. Sci., vol. 46(6), pp 1943-1947, 1999.

Castoldi A., Gatti E., Guazzoni C., Longoni A., Rehak P., and Strüder L., *The Controlled-Drift Detector*, Nucl. Instr. And Meth. A439, 519-528, January 2000a.

Castoldi A., Gatti E., Guazzoni C., Longoni A., Rehak P., Strüder L., *A new architecture of the controlled-drift detector: design and characterization*, IEEE Trans. Nucl. Sci., vol. 47(3), pp 844-850, 2000b.

Castoldi A., Cattaneo G., Galimberti A., Guazzoni C., Rehak P.,and Strüder L., *Room-Temperature 2-D X-ray Imaging with the Controlled-Drift Detector*, IEEE Trans. Nucl. Sci., Vol. 49, No.3, 989-994, June 2002.

Castoldi A., Galimberti A., Guazzoni C., and Strüder L. *Time-Resolved X-ray Spectroscopic Imaging with Novel Silicon Drift Detectors*, IEEE Trans. Nucl. Sci.,Vol 53, No. 1, February 2006.

Castoldi A., Guazzoni C., Galimberti A., Hartmann R., Pani S., Royle G., and Strüder L., *Application of Controlled-Drift Detectors in Diffraction Enhanced Imaging of Tissues*, IEEE Trans. Nucl. Sci., Vol 54, No 5, October 2007.

Chapman D, Thomlinson W, and Johnston RE, *Diffraction Enhanced X-ray Imaging*. Phys Med Biol, 42:2015-2025, 1997.

Davidson M. W., and Abramowitz M., *Concepts in Digital Imaging Technology; Two Phase CCD Clocking*, **http://micro.magnet.fsu.edu/primer/digitalimaging/concepts/twophase.html**, last accessed December 2006.

Evans S.H., Bradley D.A., Dance D.R., Bateman J.E., and Jones C.H., *Measurement of Small-Angle Photon Scattering for Some Breast Tissues and Tissue Substitute Materials*, Physics in Medicine and Biology, 36(1), 7-18, 1991.

Galimberti A., *X-ray Detection System Based on Controlled Drift Detectors for Energy Resolved Imaging with Microsecond Time Resolution*, PhD Thesis, Politecnico di Milano, 2004.

Griffiths J. A., *X-ray Diffraction Measurements for Breast Tissue Analysis*, PhD Thesis, University College London, 2005.

Guazzoni C., *The Controlled Drift Detector: A New X-ray Image Detector*, PhD Thesis, Politecnico di Milano, 1997.

Harris J., Royle G.J., Speller R.D., Griffiths J.A., Kidane G., and Hanby A.M., *Evaluation of a novel low light level (L3Vision) CCD technology for application to diffraction enhanced breast imaging*, Nuclear Instruments and Methods in Physics Research A, 513(1-2), 27-31, (2003).

Hubbell J.H., Veigele W.J., Briggs E.A., Brown R.T., Cromer D.T., and Howerton R.J., *Atomic form factors, incoherent scattering functions and photon scattering crosssections,* Journal of Physical Chemistry Reference Data, 4, 471, (1975).

Jerram P., Pool P., Bell R., Burt D., Bowring S., Spencer S., Hazelwood M., Moody I., Catlett N., and Heyes P., *The LLLCCD: low light imaging without the need for an intensifier*, in Sensors and Camera Systems for Scientific, Industrial, and Digital Photography Applications II, (SPIE, 2001), pp. 178-186.

Johns H.E., and Cunningham J.R., *The Physics of Radiology, Fourth edition*, publ. Charles C. Thomas, Springfield, Illinois, 1983.

Johns P.C., and Yaffe M.J., *X-ray Characterization of Normal and Neoplastic Breast Tissues*, Physics in Medicine and Biology, 32(6), 675-695, 1987.

Keyriläinen J, *Diffraction Enhanced X-ray Imaging of In-Vitro Breast Tumors*, PhD Thesis, University of Helsinki, 2004.

KidaneG., SpellerR.D., RoyleG.J., and Hanby A.M., *X-ray Scatter Signatures for Normal and Neoplastic Breast Tissues,* Physics in Medicine and Biology, 44(7), 1791-1802, 1999.

Lewis R. A., Rogers K. D., Hall C. J., Towns-Andrews E., Slawson S., Evans A., Pinder S. E., Ellis I. O., Boggis C. R. M., Hufton A. P., and Dance D. R., *Breast cancer Diagnosis Using Scattering X-rays,* Journal of Synchrotron Radiation, 7, 348-352, 2000.

Lutz G., *Semiconductor Radiation Detectors: Device Physics,* Springer-Verlag Berlin Heidelberg, 1999

Oppelt A., *Imaging Systems for Medical Diagnostics: Fundamentals, Technical Solutions and Applications for Systems Applying Ionizing Radiation, Nuclear Magnetic Resonance and Ultrasound, 2nd Edition,* Wiley-VCH, 2005.

Pisano E. D., Johnston R. E., Chapman D., Geradts J., Iacocca M. V., Livasy C. A., Washburn D. B., Sayers D. E., Zhong Z., Kiss M. Z., and Thomlinson W. C., *Human Breast Cancer Specimens: Diffraction-enhanced Imaging with Histologic Correlation-Improved Conspicuity of Lesion Detail Compared with Digital Radiography,* Radiology, 214, 895 - 901. March 2000.

Poletti M. E., Gonçalves O. D., and Mazzaro I., *X-ray Scattering from Human Breast Tissues and Breast-Equivalent Materials,* Physics in Medicine and Biology, 47(1), 47-63, 2002.

Rowlands J. A., *Current Advances and Future Trends in X-ray Digital Detectors,* IEEE Instr. Meas. Mag. Vol. 1, 26-28, 1998.

Roy S.C., Lynn K., and Pratt R. H., *Elastic Scattering of Photons,* Radiat. Phys. Chem., Vol. 56, pp. 3-26, 1999.

Tartari A., *Molecular Differential Cross Sections for Low Angle Photon Scattering in Tissues,* Radiation Physics and Chemistry, 56, 205-211, 1999.

Theuwissen A. J. P., *Solid-state Imaging with Charge-coupled Devices,* Illustrated Edition, Springer, 1995

Vedani G., *Sviluppo di Un Nuovo Sistema di Rivelazione di Immagini X in Diffrazione Basato su Rivelatori in Silicio a Deriva Controllata,* MS Thesis, Politecnico di Milano, 2007

Vesoci A., *Sistema di rivelazione per Diffraction Enhanced Imaging di raggi X basato su rivelatori a deriva controllata,* MS Thesis, Poltiecnico di Milano, 2005.